Available online at www.sciencedirect.com
ScienceDirect
Ocean Engineering 35 (2008) 616–636
OCEAN ENGINEERING
www.elsevier.com/locate/oceaneng

A finite differences formulation for the linear and nonlinear dynamics of 2D catenary risers

Ioannis K. Chatjigeorgiou*

Division of Marine Structures, School of Naval Architecture and Marine Engineering, National Technical University of Athens, 9 Heroön Polytechniou Ave, GR 157-73, Zografos Campus, Athens, Greece

Received 25 March 2007; accepted 3 January 2008
Available online 10 January 2008

Abstract

A finite differences (FD) solution method is proposed for the numerical treatment of the dynamic equilibrium problem of 2D catenary risers. The method is based on the so-called Box approximation, which in the scope of the present contribution is applied to the complete nonlinear model as well as to the reduced linearized formulation. The application of the Box method transforms the original governing systems into convenient sets of algebraic equations, which in turn are solved efficiently by the relaxation method. Extensive numerical calculations are presented that describe the dynamic behaviour of the structure and evaluate the amplification in loading due to the dynamic components. The effect of the geometric nonlinearities is assessed through comparative calculations that concern both mathematical formulations examined in the present, i.e. the complete nonlinear, and the reduced linearized model. Special attention is paid to the heave excitations as they amplify significantly the magnitudes of the loading components.

Keywords: Marine risers; Finite differences; Box method; Heave excitations

1. Introduction

Offshore applications for deepwater drilling, rely, one way or another, on the proper design and installation of the marine risers' system which are used for the transportation of the material from the seafloor to the storage-offloading vessel. There is currently a boom in the development of risers from universities, research institutes, third parties and offshore industries. The increased interest can be justified by the need in drilling in deeper waters. In such large depths, catenary risers are of particular importance due to their lower installation cost. Nevertheless, as it was expected, several issues came up, which are of both industry and academic interest. Some indicative examples include the riser–soil interaction effects in bottoms of practically unknown contour, the ill-understood vortex induced vibration (VIV) effects and the floater vortex induced motion (VIM) induced riser fatigue, extreme dynamic amplification of bending moments at the touch-down region, etc. Some of these issues are related to the dynamic response of the riser under imposed excitation applied at the top of the structure, which represents the motions of the floating vessel. Therefore the dynamic analysis is a key issue that requires deep and comprehensive investigation of the associated system, proper formulation of the theoretical model and finally, the use of an efficient solution method. A review on the existing methods and the analysis techniques can be found in the works of Jain (1994) and Patel and Seyed (1995).

The great majority of the proposed solution methodologies rely on the finite elements (FE) method, which appears to be the most popular. Indicative examples of relevant research efforts that cover almost two decades are the works reported by McNamara et al. (1988), Fylling et al. (1998) and Chai and Varyani (2006). Nowadays, there are several commercially available computer codes, such as Deeplines (Principia web: www.principia.fr), Flexcom (MCS web: www.mcs.com), Riflex (Sintef web: www.sintef.no) and OrcaFlex (Orcina web: www.orcina.com), which are all based on the FE approximation. Examples of alternative formulations for studying the dynamics of catenary risers can be found in the studies of Pesce et al. (1999, 2006). The authors applied a semi-analytical

*Tel.: +30 210 772 1105; fax: +30 210 772 1412.
E-mail address: chatji@central.ntua.gr

0029-8018/$ - see front matter © 2008 Elsevier Ltd. All rights reserved.
doi:10.1016/j.oceaneng.2008.01.006

formulation, which requires the solution of the associated eigenvalue problem. To this end the classical WKB approximation was employed.

FE method is not the only unadulterated numerical method, which can be used for exploring the details of the dynamic behaviour of catenary risers. Finite differences (FD) methods, although not so popular as the FE methods, can be equally efficient for solving the dynamic equilibrium problem for catenary shaped slender structures. Nevertheless, there are only few works that make use of FD methods, as it is admitted in the review reported by Patel and Seyed (1995). FD methods have been employed mainly for the solution of the static equilibrium problem (Dareing and Neathering, 1970; Zare and Datta, 1988; Jain, 1994) or as a numerical scheme for the integration in the time domain, alternative to Houbolt, Wilson-θ and Newmark-β methods (Patel and Seyed, 1995). The difficulties on the use of the FD methods arise mainly from the coupled discretization that is required in time and space, which in turn leads to complicated algebraic systems. These problems are properly addressed in the present by extending an existing FD methodology to riser type slender structures with non-zero bending stiffness. In particular, the method which is employed is the so-called Keller Box FD numerical scheme (Hoffman, 1993), known widely as the Box method.

This method was first introduced in cable dynamics by Ablow and Schechter (1983) and expanded by Milinazzo et al. (1987) who introduced a number of modifications in order to produce a more efficient and stable method of computing, applied in towed cable systems. The same method was adopted afterwards by several researchers for applications involving low tension cables (Howell, 1991), cable deployment (Burgess, 1993), highly extensible cables (Tjavaras et al., 1998) and nonlinear dynamics of vertical slender structures (Chatjigeorgiou, 2004). Here the method is properly extended for developing an FD numerical scheme for the solution of the 2D dynamic equilibrium problem of catenary risers.

The numerical predictions, which are presented in the sequel, concentrate mainly on the characteristics of the bending vibration problem. Thus, particular attention is paid on the transversal motions and the associated bending moments. The contribution of the nonlinear effects is assessed through comparative calculations between the complete nonlinear and the equivalent linearized system. The numerical treatment of the linearized system is carried out using a reduced centred differences scheme.

2. Mathematical formulation

The 2D nonlinear dynamic problem of a catenary riser is considered. The riser is modelled as a hinged–hinged slender structure (Fig. 1). The mass, the added mass and the submerged weight per unit unstretched length are denoted by m, m_a and w_0, respectively, while EA and EI are the elastic stiffness and the flexural rigidity. The governing system that describes the 2D dynamic behaviour of a

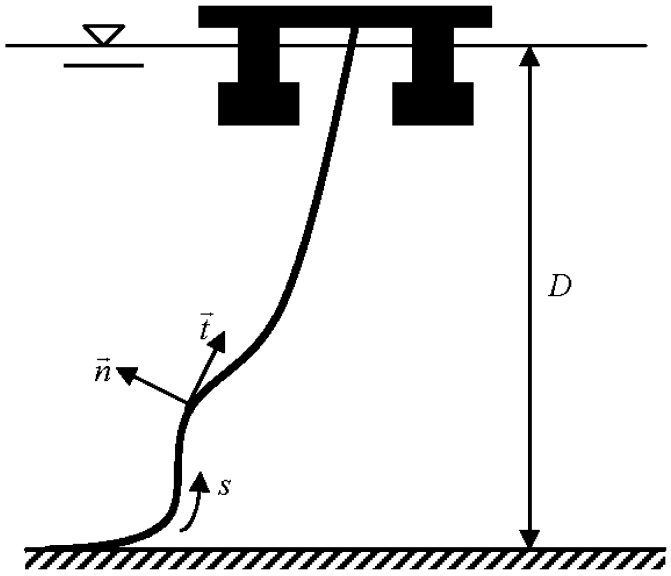

Fig. 1. Coordinate systems for the 2D dynamic problem of a catenary riser.

catenary riser is composed by the following six nonlinear partial differential equations (Trianrafyllou, 1994):

$$m\left(\frac{\partial u}{\partial t}-v\frac{\partial \phi}{\partial t}\right)=\frac{\partial T}{\partial s}-w_0\sin\phi-\Omega Q-\frac{1}{2}\rho\pi C_{dt}\,d|u_r|u_r, \tag{1}$$

$$m\left(\frac{\partial v}{\partial t}+u\frac{\partial \phi}{\partial t}\right)+m_a\frac{\partial v_r}{\partial t}=\frac{\partial Q}{\partial s}+T\Omega-w_0\cos\phi-\frac{1}{2}\rho C_{dn}\,d|v_r|v_r, \tag{2}$$

$$\frac{\partial T}{\partial t}=EA\left(\frac{\partial u}{\partial s}-v\Omega\right), \tag{3}$$

$$\frac{\partial \phi}{\partial t}=\frac{\partial v}{\partial s}+u\Omega, \tag{4}$$

$$EI\frac{\partial \Omega}{\partial s}=-Q, \tag{5}$$

$$\frac{\partial \phi}{\partial s}=\Omega, \tag{6}$$

where s is the unstretched Lagragian coordinate and t is the time. The cross-sectional area A and the moment of inertia I, are calculated in terms of the unstretched inner and outer diameters. The vector of the unknowns $\mathbf{Y}=[T,Q,u,v,\Omega,\phi]^{\mathrm{T}}$ is composed of the velocities u and v in the tangential $\vec{t}$ and transversal direction $\vec{n}$, respectively (see Fig. 1), the tension T, the angle ϕ which is formed between the tangent on the structure and the horizontal, the shear force Q and the curvature Ω. Here, T, ϕ, Q and Ω represent total quantities, i.e. the summation of the static and the dynamic components. The last terms in the right-hand side of Eqs. (1) and (2) are the quadratic drag forces parallel to $\vec{t}$ and $\vec{n}$ and they are

expressed in terms of the relative velocities u_r and v_r when a steady current is presented. In the present work no current was considered and consequently u_r and v_r are directly replaced by u and v. In the adopted Morison's formula, d denotes the unstretched external diameter of the riser, $\rho = 1025\,\mathrm{kg/m^3}$ is the seawater density while C_{dt} and C_{dn} are the drag coefficients in the tangential and normal direction, respectively. Eq. (3) assumes a linear stress–strain relation. In most of the cases, catenary risers are made from steel. Although a nonlinear stress–strain relation has no physical essence for steel catenary risers, the above formulation can be easily extended in order to incorporate relevant contributions.

3. Nonlinear problem—solution in the time domain

Eqs. (1)–(6) are treated without applying any additional assumption regarding the contribution of the various terms. This system is solved by employing the Keller Box FD method. The Box approximation is implicit, two level, single step, unconditionally stable and convergent. The major advantage of this method is that the physical grid spacing can be non-uniform. Nevertheless, this capability is not used in the present formulation as the configuration of the structure does not involve any geometrical discontinuities, which would require denser grid.

First, the original system (1)–(6) is rewritten in the following convenient vectorial form:

$$\frac{\partial \mathbf{Y}}{\partial s} = \frac{\partial \mathbf{Y}}{\partial t} + \mathbf{F}, \tag{7}$$

where

$$\frac{\partial \mathbf{Y}}{\partial s} = \frac{\partial}{\partial s}[T \;\; Q \;\; EAu \;\; v \;\; EI\,\Omega \;\; \phi]^{\mathrm{T}}, \tag{8}$$

$$\frac{\partial \mathbf{Y}}{\partial t} = \frac{\partial}{\partial t}[mu \;\; (m+m_a)v \;\; T \;\; \phi \;\; 0 \;\; 0]^{\mathrm{T}}, \tag{9}$$

$$\mathbf{F} = \begin{bmatrix} -mv\dfrac{\partial \phi}{\partial t} + w_0 \sin\phi + \Omega Q + \dfrac{1}{2}\rho\pi C_{dt} d|u|u \\ mu\dfrac{\partial \phi}{\partial t} - T\Omega + w_0 \cos\phi + \dfrac{1}{2}\rho C_{dn} d|v|v \\ EAv\Omega \\ -u\Omega \\ -Q \\ \Omega \end{bmatrix}. \tag{10}$$

Next, Eq. (7) is evaluated at $[k-1/2,\ j+1/2]$ where the indexes k and j are used to denote the discretization in space and time, respectively. Thus, Eq. (7) obtains the following algebraic form:

$$\frac{\mathbf{Y}_k^{j+1} + \mathbf{Y}_k^{j} - \mathbf{Y}_{k-1}^{j+1} - \mathbf{Y}_{k-1}^{j}}{2\Delta s} = \frac{\mathbf{Y}_k^{j+1} + \mathbf{Y}_{k-1}^{j+1} - \mathbf{Y}_k^{j} - \mathbf{Y}_{k-1}^{j}}{2\Delta t} + \frac{1}{4}(\mathbf{F}_k^{j+1} + \mathbf{F}_{k-1}^{j+1} + \mathbf{F}_k^{j} + \mathbf{F}_{k-1}^{j}). \tag{11}$$

The complete algebraic expansions of Eqs. (1)–(6) are given in Appendix A. In Eq. (11), $j+1$ denotes the time step in which the solution is required. The moment j is the previous step where the time dependent variables are already known and in addition they were used as the first guess in the iterative process. At $t = 0$, $\mathbf{Y}_k^j$ is replaced by the static values.

Assuming that the unstretched suspended length of the catenary is discretized using n equally spaced points, the system of algebraic equations represented by Eq. (11) is evaluated at all points from $k = 2$ through $k = n$, providing a system of $6(n-1)$ algebraic equations. This system is supplemented by the six boundary conditions, which must be enforced at the ends of the riser. Due to the implicit nature of the FD equations, the final $6n$ system must be solved simultaneously. This is carried out by the relaxation method (Press et al., 1986). The boundary conditions associated with riser's operation should guarantee that the bending moments, or alternatively the curvatures, at both ends are zero. In addition, it is considered that the lower attachment point is fixed while the velocities at the top are expressed as predefined functions of time. Using the notations adopted before, the boundary conditions are expressed as

$$\Omega_1^{j+1} = 0, \quad \Omega_n^{j+1} = 0, \quad u_1^{j+1} = 0, \quad v_1^{j+1} = 0,$$
$$u_n^{j+1} = u_a(t), \quad v_n^{j+1} = v_a(t). \tag{12}$$

4. Linear system—solution in the frequency domain

Although the solution of the equivalent linearized problem seems easier, it involves several practical difficulties as the employed numerical methodology should be applied to 12 differential equations instead of the six equations of the complete nonlinear system. The fundamental assumption that enables the derivation of the equivalent linearized system is that the vector of the unknowns is composed of a static and a dynamic part. Thus,

$$\mathbf{Y}(s,t) = \overline{\mathbf{Y}}(s) + \widetilde{\mathbf{Y}}(s,t), \tag{13}$$

where the static and the dynamic terms of the right-hand side of Eq. (13) are given by

$$\overline{\mathbf{Y}}(s) = [\overline{T}(s), \overline{Q}(s), 0, 0, \overline{\Omega}(s), \overline{\phi}(s)]^{\mathbf{T}}, \tag{14}$$

$$\widetilde{\mathbf{Y}}(s,t) = [\widetilde{T}(s,t), \widetilde{Q}(s,t), p(s,t), q(s,t), \widetilde{\Omega}(s,t), \widetilde{\phi}(s,t)]^{\mathbf{T}}. \tag{15}$$

Here the displacements along the structure are expressed as motions instead of velocities as it was carried out for the complete nonlinear system. In Eq. (15) $p(s,t)$ and $q(s,t)$ denote the axial and transversal motions, respectively, given by $u(s,t) = \partial p(s,t)/\partial t$ and $v(s,t) = \partial q(s,t)/\partial t$. Next, Eqs. (13)–(15) are introduced into the governing set of Eqs. (1)–(6). From the resulting system we ignore all nonlinear terms, except the equivalent linearized form of the drag force in transversal direction. The terms that

describe the static equilibrium problem are also omitted. Thus, the original system is reduced to

$$m\frac{\partial^2 p}{\partial t^2}=\frac{\partial \widetilde{T}}{\partial s}-w_0\cos\overline{\phi}\widetilde{\phi}-\overline{Q}\widetilde{\Omega}-\widetilde{\Omega}\overline{\Omega}, \tag{16}$$

$$(m+m_a)\frac{\partial^2 q}{\partial t^2}=\frac{\partial \widetilde{Q}}{\partial s}+w_0\sin\overline{\phi}\widetilde{\phi}+\overline{T}\widetilde{\Omega}+\widetilde{T}\overline{\Omega}-b_0\omega|q|\frac{\partial q}{\partial t}, \tag{17}$$

$$\widetilde{T}=EA\left(\frac{\partial p}{\partial s}-\overline{\Omega}q\right), \tag{18}$$

$$\widetilde{\phi}=\frac{\partial q}{\partial s}+\overline{\Omega}p, \tag{19}$$

$$\widetilde{Q}=-EI\frac{\partial \widetilde{\Omega}}{\partial s}, \tag{20}$$

$$\widetilde{\Omega}=\frac{\partial \widetilde{\phi}}{\partial s}. \tag{21}$$

In Eq. (17), ω denotes the frequency of the response, which in the scope of the linear problem is equal to the excitation frequency. Furthermore $b_0=4/(3\pi)\rho C_{dn}d$ is the linearized damping coefficient which is determined through the linearization process.

The solution in the frequency domain requires that the vector of the unknown dynamic components $\tilde{\mathbf{Y}}(s,t)$ should be expressed as

$$\overline{\mathbf{Y}}(s,t)=\{\mathrm{Re}\,\widetilde{\mathbf{y}}(s)e^{i\omega t}\},$$
$$\tilde{y}(s)=[\widetilde{T}(s),\widetilde{Q}(s),p(s),q(s),\widetilde{\Omega}(s),\widetilde{\phi}(s)]^{\mathbf{T}}, \tag{22}$$

where the spatial vector $\widetilde{\mathbf{y}}(s)$ is given by the following complex form:

$$\widetilde{\mathbf{y}}(s)=\widetilde{\mathbf{y}}^{(r)}(s)+i\widetilde{\mathbf{y}}^{(i)}(s). \tag{23}$$

Apparently, the indexes (r) and (i) denote the real and imaginary part, respectively. After introducing Eqs. (22) and (23) into Eqs. (16)–(21), the original linearized system is transformed into a reduced spatially dependent system which after separating real and imaginary parts is recast into the following matrix form:

$$\begin{bmatrix}\frac{d\widetilde{T}^{(r)}}{ds}\\ \frac{d\widetilde{T}^{(i)}}{ds}\\ \frac{d\widetilde{Q}^{(r)}}{ds}\\ \frac{d\widetilde{Q}^{(i)}}{ds}\\ \frac{dp^{(r)}}{ds}\\ \frac{dp^{(i)}}{ds}\\ \frac{dq^{(r)}}{ds}\\ \frac{dq^{(i)}}{ds}\\ \frac{d\widetilde{Q}^{(r)}}{ds}\\ \frac{d\widetilde{Q}^{(i)}}{ds}\\ \frac{d\widetilde{\phi}^{(r)}}{ds}\\ \frac{d\widetilde{\phi}^{(i)}}{ds}\end{bmatrix}+\begin{bmatrix}0&0&-\overline{\Omega}&0&\omega^2m&0&0&0&-\overline{Q}&0&-w_0\cos\overline{\phi}&0\\ 0&0&0&-\overline{\Omega}&0&\omega^2m&0&0&0&-\overline{Q}&0&-w_0\cos\overline{\phi}\\ \bar{\Omega}&0&0&0&0&0&\omega^2(m+m_a)&b_0\omega^2|q|&\overline{T}&0&w_0\sin\overline{\phi}&0\\ 0&\bar{\Omega}&0&0&0&0&-b_0\omega^2|q|&\omega^2(m+m_a)&0&\overline{T}&0&w_0\sin\overline{\phi}\\ -\frac{1}{EA}&0&0&0&0&0&-\overline{\Omega}&0&0&0&0&0\\ 0&-\frac{1}{EA}&0&0&0&0&0&-\overline{\Omega}&0&0&0&0\\ 0&0&0&0&\overline{\Omega}&0&0&0&0&0&-1&0\\ 0&0&0&0&0&\overline{\Omega}&0&0&0&0&0&-1\\ 0&0&\frac{1}{EI}&0&0&0&0&0&0&0&0&0\\ 0&0&0&\frac{1}{EI}&0&0&0&0&0&0&0&0\\ 0&0&0&0&0&0&0&0&-1&0&0&0\\ 0&0&0&0&0&0&0&0&0&-1&0&0\end{bmatrix}\bullet\begin{bmatrix}\widetilde{T}^{(r)}\\ \widetilde{T}^{(i)}\\ \widetilde{Q}^{(r)}\\ \widetilde{Q}^{(i)}\\ p^{(r)}\\ p^{(i)}\\ q^{(r)}\\ q^{(i)}\\ \widetilde{\Omega}^{(r)}\\ \widetilde{\Omega}^{(i)}\\ \widetilde{\phi}^{(r)}\\ \widetilde{\phi}^{(i)}\end{bmatrix}=0. \tag{24}$$

Eq. (24) represents a system of 12 ordinary differential equations, which can be treated by employing a reduced centred differences scheme. According to this scheme all equations are evaluated at all $n-1$ discetization points along the catenary, from $k=2$ to $k=n$, and a system that consists of $12(n-1)$ algebraic equations is derived. This system must be supplemented by the 12 boundary conditions, which must be enforced at the ends of the structure. The solution of the final $12n$ algebraic equations is carried out using the relaxation method (Press et al.,

1986). The boundary conditions associated with the linear problem are expressed mathematically as

$$p_n^{(r)} = p_{a0}, \quad p_n^{(i)} = 0, \quad q_n^{(r)} = q_{a0},$$
$$q_n^{(i)} = 0, \quad \widetilde{\Omega}_n^{(r)} = 0, \quad \widetilde{\Omega}_n^{(i)} = 0, \tag{25}$$

$$p_1^{(r)} = 0, \quad p_1^{(i)} = 0, \quad q_1^{(r)} = 0, \quad q_1^{(i)} = 0,$$
$$\widetilde{\Omega}_1^{(r)} = 0, \quad \widetilde{\Omega}_1^{(i)} = 0, \tag{26}$$

where p_{a0} and q_{a0} are the amplitudes of the axial and transversal harmonic motions which are imposed at the top of the structure. The algebraic expansion of Eq. (24) is given in Appendix B.

5. Numerical results

The numerical results, which are presented and discussed in this section, concern a riser which has an outer diameter 42.0 cm, 2.2 cm wall thickness and thus an inner diameter 38.5 cm, approx. 15 in. An outer coating of slight buoyant material was added along the riser while its contents have a density of 200 kg/m^3, corresponding to gas. The properties of the structures, which are investigated in the present are given in Table 1. The two first models were taken from the work of Passano and Larsen (2006), while the third is used for exploring the effect of small depths on the contributions that originate from the geometric nonlinear terms. This is discussed at the end of the paper. The first two models correspond to nearly vertical configurations as can be easily seen by the sufficiently small angles, which are formed between the tangent of the risers at the top, and the perpendicular. Results from the static equilibrium problems are given in Figs. 2 and 3. Fig. 2 shows the variation of the static tension and the static bending moment as a function of the unstretched Lagragian coordinate s and Fig. 3 depicts the catenary configurations with respect to the inertia coordinate system (x–z) fixed on the touch-down point. The static tension curves (Fig. 2) have been divided

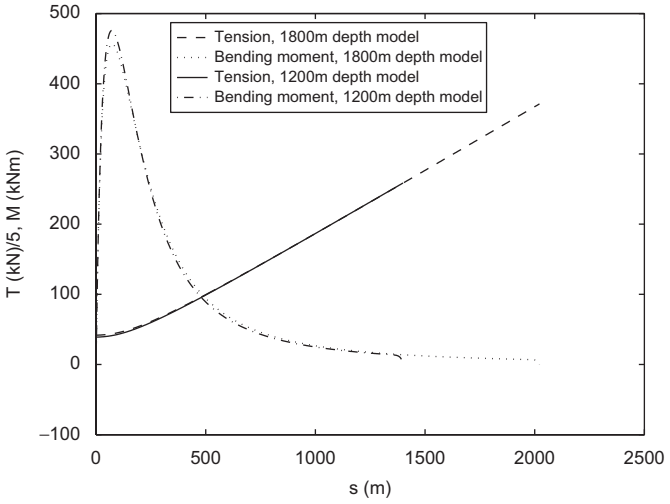

Fig. 2. Results from the static equilibrium problem: static tension and static bending moment.

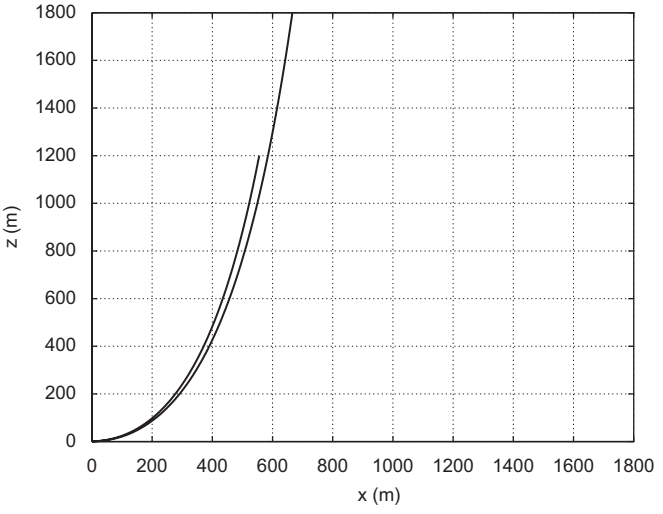

Fig. 3. Results from the static equilibrium problem: configuration of the catenaries for the 1800 and 1200 m depth models.

Table 1
Riser properties

		Model no. 1	Model no. 2	Model no. 3
Suspended length	L (m)	2022	1400	316
Outer diameter	d_o (m)	0.429	0.429	0.429
Inner diameter	d_i (m)	0.385	0.385	0.385
Mass per unit length	M (kg/m)	262.933	262.933	262.933
Added mass coefficient	C_a	1.0	1.0	1.0
Weight per unit length	w_0 (N/m)	915.56	915.56	915.56
Elastic stiffness	EA (N)	0.5823×10^{10}	0.5823×10^{10}	0.5823×10^{10}
Bending stiffness	EI (N m^2)	0.1209×10^{9}	0.1209×10^{9}	0.1209×10^{9}
Normal drag coefficient	C_{dn}	1.0	1.0	1.0
Tangential drag coefficient	C_{dt}	0.0	0.0	0.0
Depth	D (m)	1800	1200	100
Pretension at the top	T_p (kN)	1860	1297	500
Angle at the top with respect to perpendicular		6.2°	8.8°	55.7°

by 5 in order to fit into the plot. In fact, the majority of the calculations presented in the sequel correspond to the second riser of Table 1 while the first is used mainly for validating the efficacy of the present FD formulation in providing reliable numerical predictions. The second model, which consumes the greater part of the discussion, was purposely selected for investigating the impact of the heave motions, which are of particular importance in practical applications. The small angle, which is formed at the top of the structure (8.8°), implies that the motions imposed in vertical direction can be regarded with sufficient accuracy as axial excitations. As mentioned in API standards, axial motions are known to stimulate extreme dynamic phenomena in catenary moorings. As far as the riser type structures are concerned, axial motions are very effective on the dynamic amplification of the bending moment especially at the touch-down region. The correlation between the velocity component of the axial motions and the extreme bending moments that occur very close to the lower end of catenary risers, was studied recently by Passano and Larsen (2006). Therefore, it is interesting to investigate how the impact of the very important heave motions is reflected on the global dynamic behaviour of the riser when they act as an axial excitation. An equally critical point that requires attention is the study of the relative significance of the ordinary source of bending vibrations, namely, the conditions that generate displacements in surge direction. All these problems are properly addressed in Section 5.2.

5.1. Validation of the solution method

The results obtained by the present FD formulation have been validated against the numerical predictions of the linear module of the FE computer code RIFLEX.

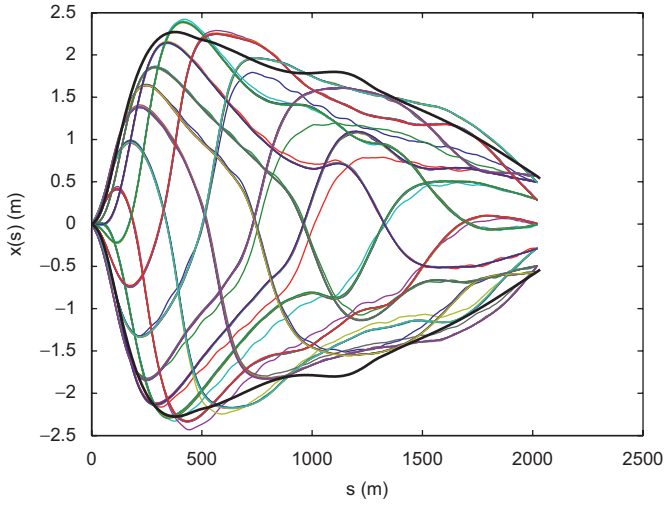

Fig. 4. Comparative results for the horizontal motion along the riser under *axial* excitation with amplitude $p_a = 5$ m and period 60 s. Snapshots where obtained using the present FD method. The envelope curves (heavy black lines) depict the maximum and minimum values calculated by RIFLEX.

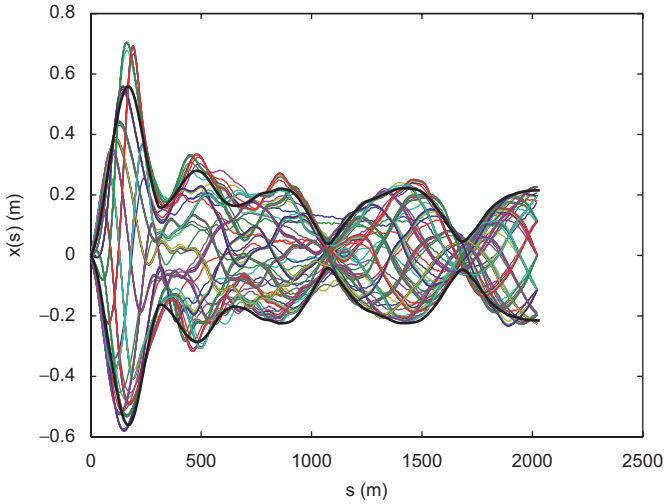

Fig. 5. Comparative results for the horizontal motion along the riser under *axial* excitation with amplitude $p_a = 2$ m and period 12 s. Snapshots where obtained using the present FD method. The envelope curves (heavy black lines) depict the maximum and minimum values calculated by RIFLEX.

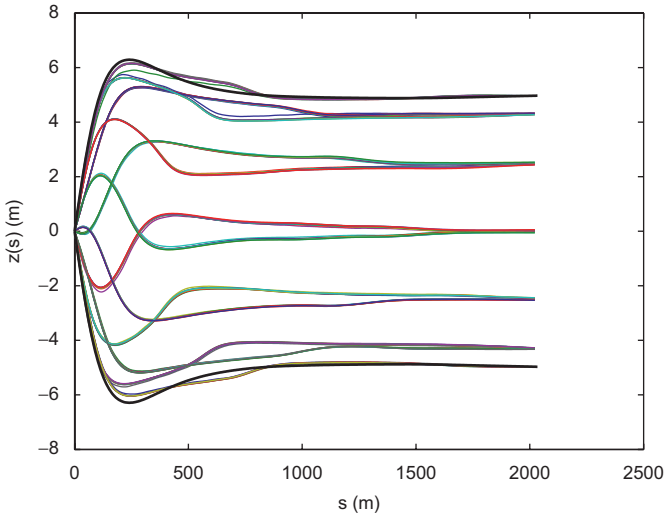

Fig. 6. Comparative results for the vertical motion along the riser under *axial* excitation with amplitude $p_a = 5$ m and period 60 s. Snapshots where obtained using the present FD method. The envelope curves (heavy black lines) depict the maximum and minimum values calculated by RIFLEX.

Additional comparative calculations with RIFLEX can be found in the work reported by Chatjigeorgiou et al. (2007). Figs. 4–9 show dynamic calculations for the first structural model of Table 1. The numerical predictions depict the horizontal motion (Figs. 4 and 5), the vertical motion (Figs. 6 and 7) and the bending moment (Figs. 8 and 9) along the structure, for two different conditions of axial loading, namely, 5 m amplitude with period 60 s (Figs. 4, 6 and 8) and 2 m amplitude with period 12 s (Figs. 5, 7 and 9). The snapshots were obtained by the nonlinear FD formulation and correspond to successive time steps that fall into a period of the steady-state response, while the envelope curves depict the numerical

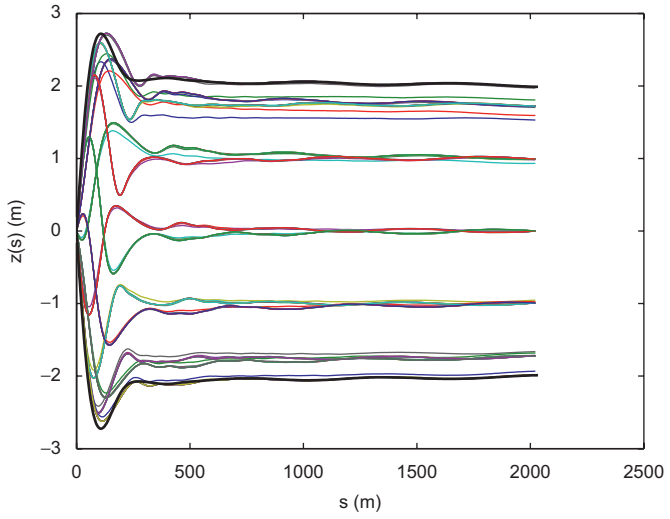

Fig. 7. Comparative results for the vertical motion along the riser under *axial* excitation with amplitude $p_a = 2$ m and period 12 s. Snapshots where obtained using the present FD method. The envelope curves (heavy black lines) depict the maximum and minimum values calculated by RIFLEX.

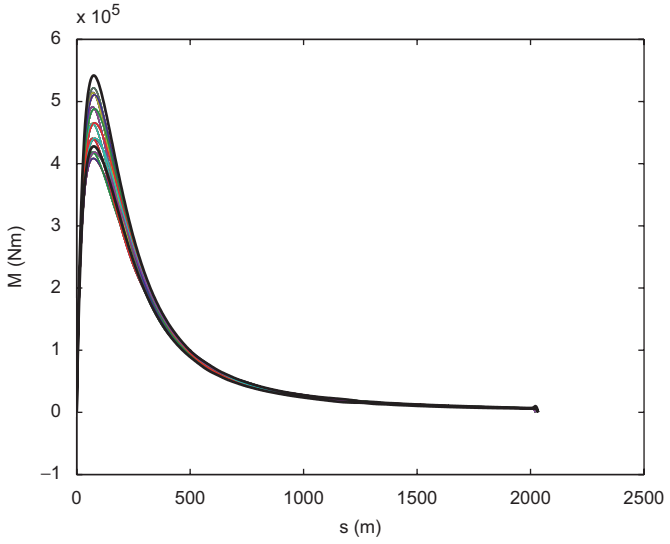

Fig. 8. Comparative results for the total bending moment along the riser under *axial* excitation with amplitude $p_a = 5$ m and period 60 s. Snapshots where obtained using the present FD method. The envelope curves (heavy black lines) depict the maximum and minimum values calculated by RIFLEX.

data calculated by RIFLEX. The FD method was applied using 400 discretization points and the time step for the solution of the problem in the time domain was set equal to 0.2 s. It is immediately apparent that the comparison of the results is very favourable. The favourable coincidence is demonstrated also in Table 2, which compares explicitly the max and min values of the bending moment and the tension at specific locations of the catenary riser and for two different conditions of axial excitation. The bending moment corresponds to the location of the maximum static bending moment which for the 2022 m long model occurs

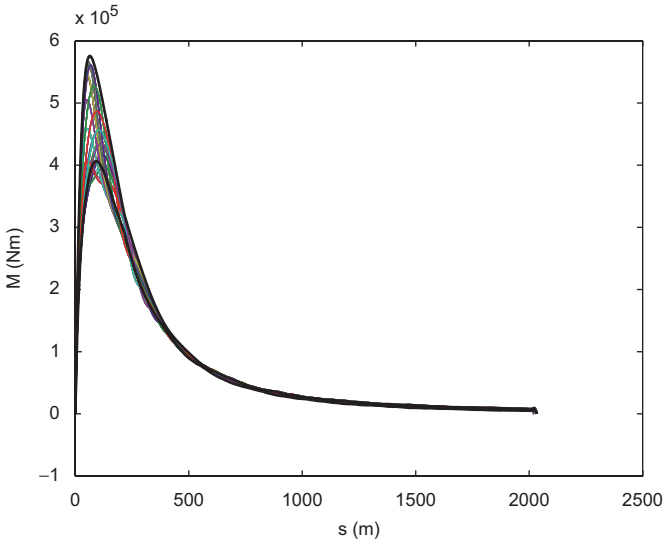

Fig. 9. Comparative results for the total bending moment along the riser under *axial* excitation with amplitude $p_a = 2$ m and period 12 s. Snapshots where obtained using the present FD method. The envelope curves (heavy black lines) depict the maximum and minimum values calculated by RIFLEX.

Table 2
Comparative results between the present FD method and RIFLEX

	$p_a = 5$ m, $T = 60$ s		$p_a = 2$ m, $T = 12$ s	
	RIFLEX	FD	RIFLEX	FD
Max tension (kN)	1895	1894	2193	2261
Min tension (kN)	1825	1825	1542	1451
Max bending moment (kN m)	542	517	575	555
Min bending moment (kN m)	428	401	406	374

at approximately $s = 74.2$ m, where s denotes the arc length from the touch-down point along the catenary. On the other hand, the tension values given in Table 2 refer to the top of the structure. The small discrepancies observed in Table 2 are most probably due to the fact that the RIFLEX predictions were obtained using the linear module.

The fast convergence of the FD method is proven by the relatively low CPU time that is required for running the computer code. For the first model of Table 1 for instance, and for a lateral excitation with amplitude 5 m and excitation period 60 s, the fully nonlinear module of RIFLEX with 600 discretization elements required 89.94 s CPU to simulate 900 s of dynamic response. The time step for this application was 0.4 s (Passano, 2007). The corresponding CPU time for the present FD method using 600 nodes and the same time step was 107.3 s in a PC. This figure drops to 31.9 s when the code runs in a powerful HP Alpha server ES45 UNIX machine.

With regard to the properties of the excitation, it is evident that the condition that corresponds to the higher axial velocity, i.e. $p_a = 2$ m with period 12 s, causes a heavier amplification of the dynamic components although the imposed amplitude is smaller. This is easily seen in the

wider area of the variation of the total bending moment just after the touch-down point (Fig. 9).

5.2. Discussion on the dynamic behaviour of catenary risers

The calculations and the discussion that follow refer to the second catenary riser (Model No 2) of Table 1. The details of its dynamic response are investigated extensively using two different amplitudes and two directions for the top imposed excitation. More specifically, the amplitudes were set equal to 1 and 2 m for both the horizontal and the vertical direction. The numerical predictions that concern all dynamic components that govern the dynamic behaviour of the riser are shown in Figs. 10–35. All calculations were performed using 400 discretization points which correspond to a node spacing $\Delta s \approx 3.5$ m, while particular

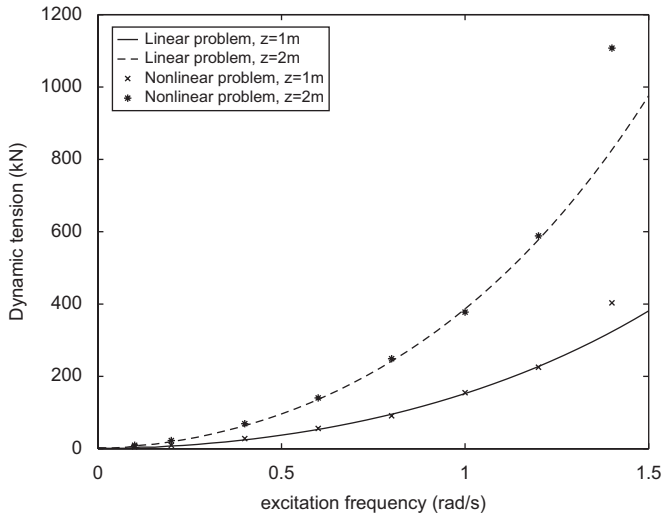

Fig. 10. Dynamic tension $\widetilde{T}$ at the location of the maximum static bending moment near the touch-down point for *heave* excitation.

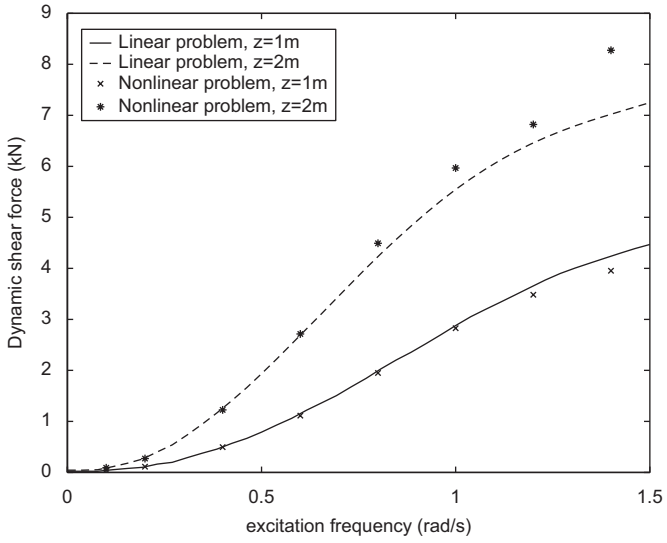

Fig. 11. Dynamic shear force $\widetilde{Q}$ at the location of the maximum static bending moment near the touch-down point for *heave* excitation.

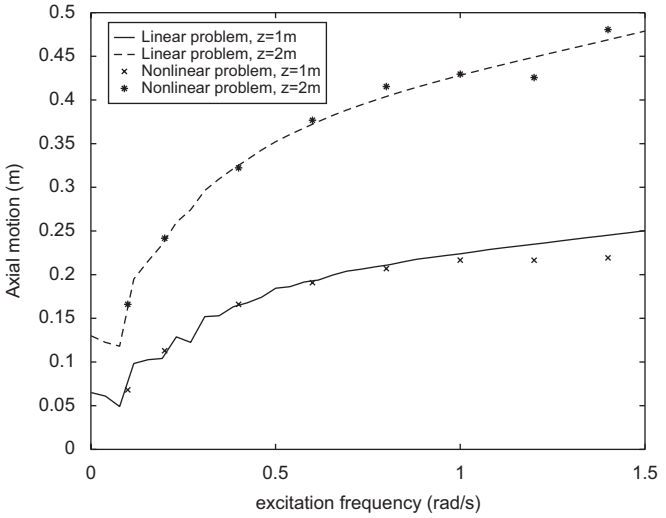

Fig. 12. Axial motion p at the location of the maximum static bending moment near the touch-down point for *heave* excitation.

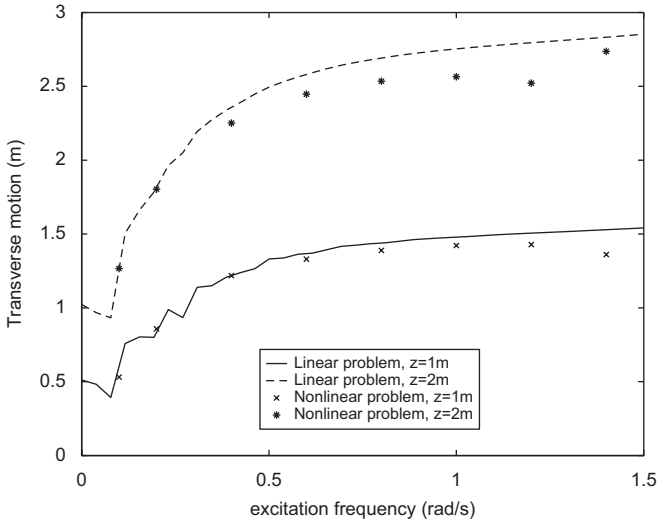

Fig. 13. Transverse motion q at the location of the maximum static bending moment near the touch-down point for *heave* excitation.

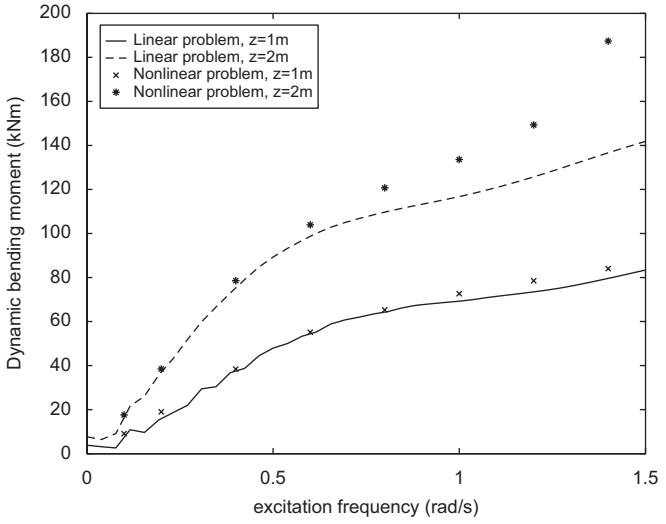

Fig. 14. Dynamic bending moment $EI\widetilde{\Omega}$ at the location of the maximum static bending moment near the touch-down point for *heave* excitation.

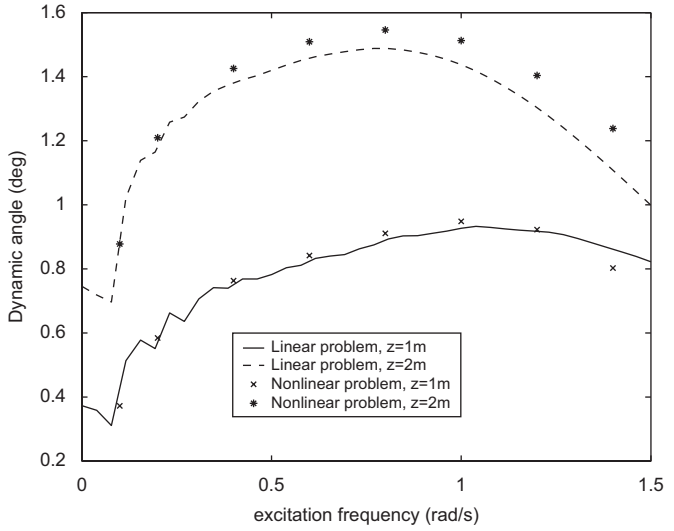

Fig. 15. Dynamic angle $\widetilde{\phi}$ at the location of the maximum static bending moment near the touch-down point for *heave* excitation.

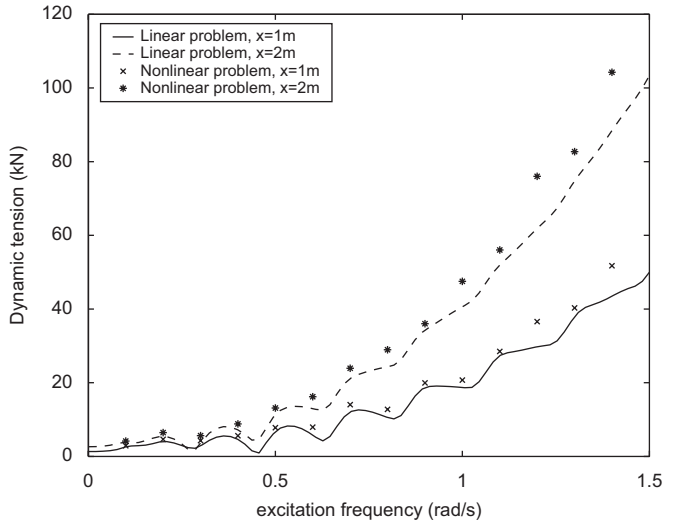

Fig. 16. Dynamic tension $\widetilde{T}$ at the location of the maximum static bending moment near the touch-down point for *surge* excitation.

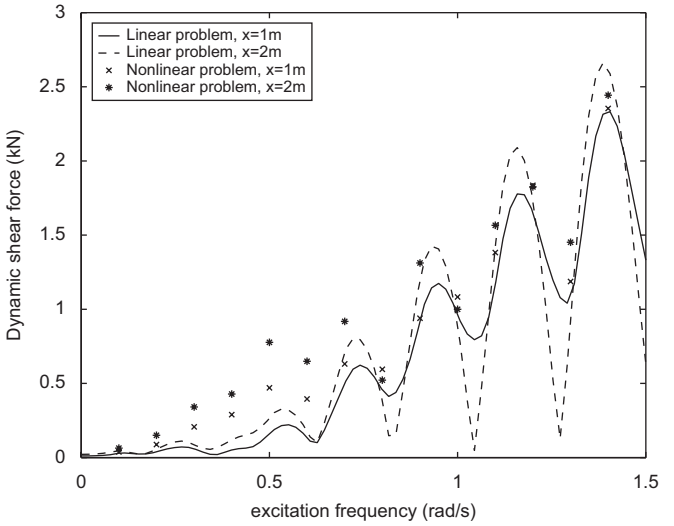

Fig. 17. Dynamic shear force $\widetilde{Q}$ at the location of the maximum static bending moment near the touch-down point for *surge* excitation.

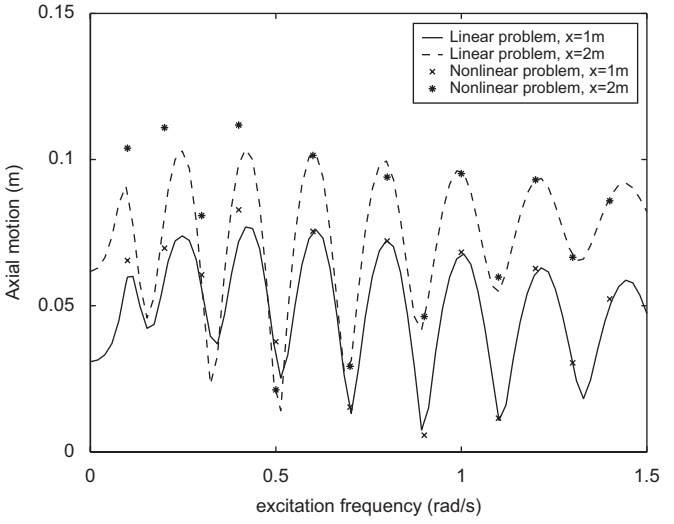

Fig. 18. Axial motion p at the location of the maximum static bending moment near the touch-down point for *surge* excitation.

attention is paid at the location of the maximum bending moment which for the specific structure occurs at the 21st node, at approximately $s=70$ m, from the touch down. With regard to the time step that was used for the solution of the equivalent algebraic system of the nonlinear partial differential equations, it was varying from $\Delta t=1$ s for the lowest frequency considered, i.e. 0.1 rad/s, to $\Delta t=0.1$ s for the highest frequency, i.e. 1.4 rad/s. The strong stability characteristics and the convergence properties of the Box method allow the use of higher values for Δs and Δt, enabling very fast solutions with negligible loss in accuracy. The afore-mentioned values were chosen rather for practical reasons, namely for producing smoother t ime histories for the description of the variation of the dynamic components along the catenary. The stability characteristics of the Box method are discussed briefly through comparative calculations in Section 5.3 of the present.

5.2.1. *Vertical excitation*

The dynamic behaviour of the second model under forced excitation in heave direction is examined with the aid of Figs. 10–15. The figures depict the transfer functions of all dynamic components that form the associated dynamic equilibrium problem. The transfer functions were obtained using the above-described frequency domain solution technique. For direct comparison and for assessing the contribution of the nonlinear effects, the linear calculations have been plotted against the numerical predictions of the complete nonlinear problem (see Eqs. (1)–(6)). The depicted data correspond to the location where the maximum static bending moment occurs, namely

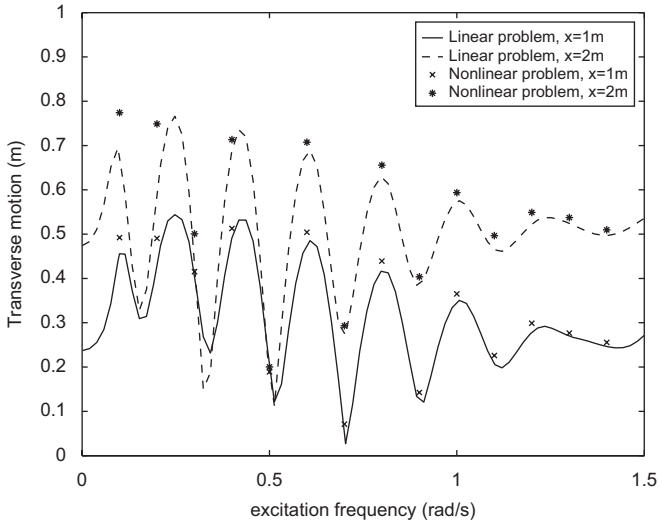

Fig. 19. Transverse motion q at the location of the maximum static bending moment near the touch-down point for *surge* excitation.

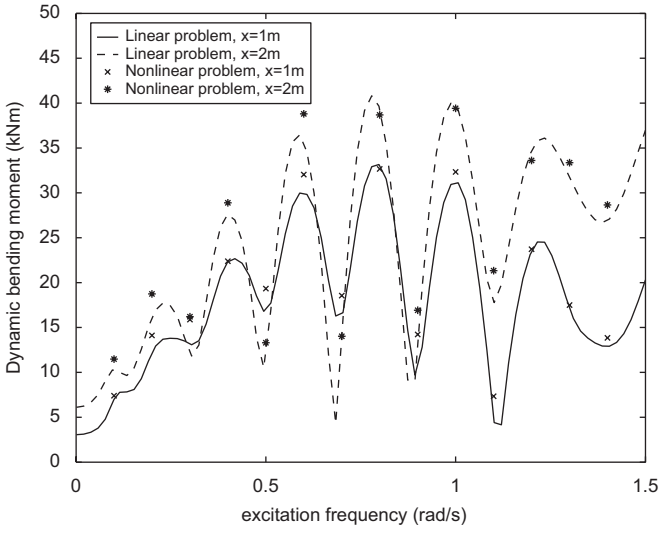

Fig. 20. Dynamic bending moment $EI\widetilde{\Omega}$ at the location of the maximum static bending moment near the touch-down point for *surge* excitation.

at the 21st node from the bottom. The persistence on this point is due to the importance of the magnitude of the maximum bending moment on the safe operation of a marine riser.

From a quick inspection of Figs. 10–15 it is easily seen that both solution methodologies provide comparable results. Noteworthy differences are observed at the end of the frequency range, which in turn implies that the relative contribution of the nonlinear effects is increased for fast excitations and for larger top end displacements. The latter remark complies with the findings of Passano and Larsen (2006) who reported that the dynamic amplification of the bending moment is correlated with the velocity of the forced excitation. The differences are more detectable in the loading components, i.e. tension (Fig. 10), shear force (Fig. 11) and bending moment (Fig. 14). Fig. 10 shows that the variation of the dynamic tension follows a catenary

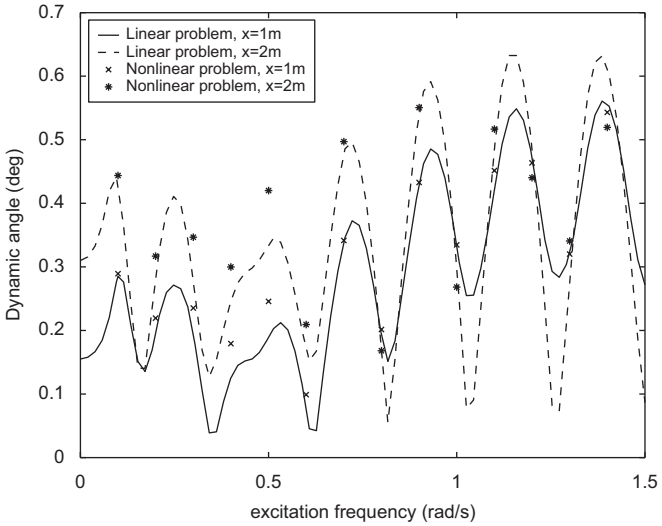

Fig. 21. Dynamic angle $\widetilde{\phi}$ at the location of the maximum static bending moment near the touch-down point for *surge* excitation.

path with increasing slope at the end of the frequency range. On the contrary, the shear force and the bending moment exhibit a different trend, which is characterized by the smaller incremental tendency for high excitation frequencies. Apparently, the above discussion concerns only the results from the linear problem while the numerical predictions that have been derived using the complete nonlinear model imply that the linearization of the system underestimate the magnitude of the loading components.

5.2.2. *Horizontal excitation*

Details on the variation of the dynamic components for horizontal top imposed excitation are depicted in Figs. 16–21. The plotted data show the magnitudes of the dynamic amplification at the location of the maximum static bending moment. It is reminded that the static configuration of the riser is almost vertical and as a result, the surge excitation can be regarded with sufficient accuracy as a transversely imposed motion.

The first conclusion that can be drawn is that the magnitudes of the dynamic components due to surge excitation are relatively insignificant when compared to the heave excitation cases for the same excitation properties. By comparing the tension curves in Figs. 10 and 16 for heave and surge excitation, respectively, we can easily deduce that the tension values are approximately 10 times smaller when the riser is excited in surge direction. Furthermore, the dynamic bending moment at the location of interest rises up to 180 kN m for heave motions (Fig. 14) while the maximum amplification for surge excitation is only 40 kN m (Fig. 20). The extreme difference in tension is a logical sequent, which originates from the extensibility of the structure. On the other hand, although the difference in bending moment is not so profound, the specific variable is more illustrative of the severity of the heave motions on the dynamic behaviour of the riser. Taking into account the

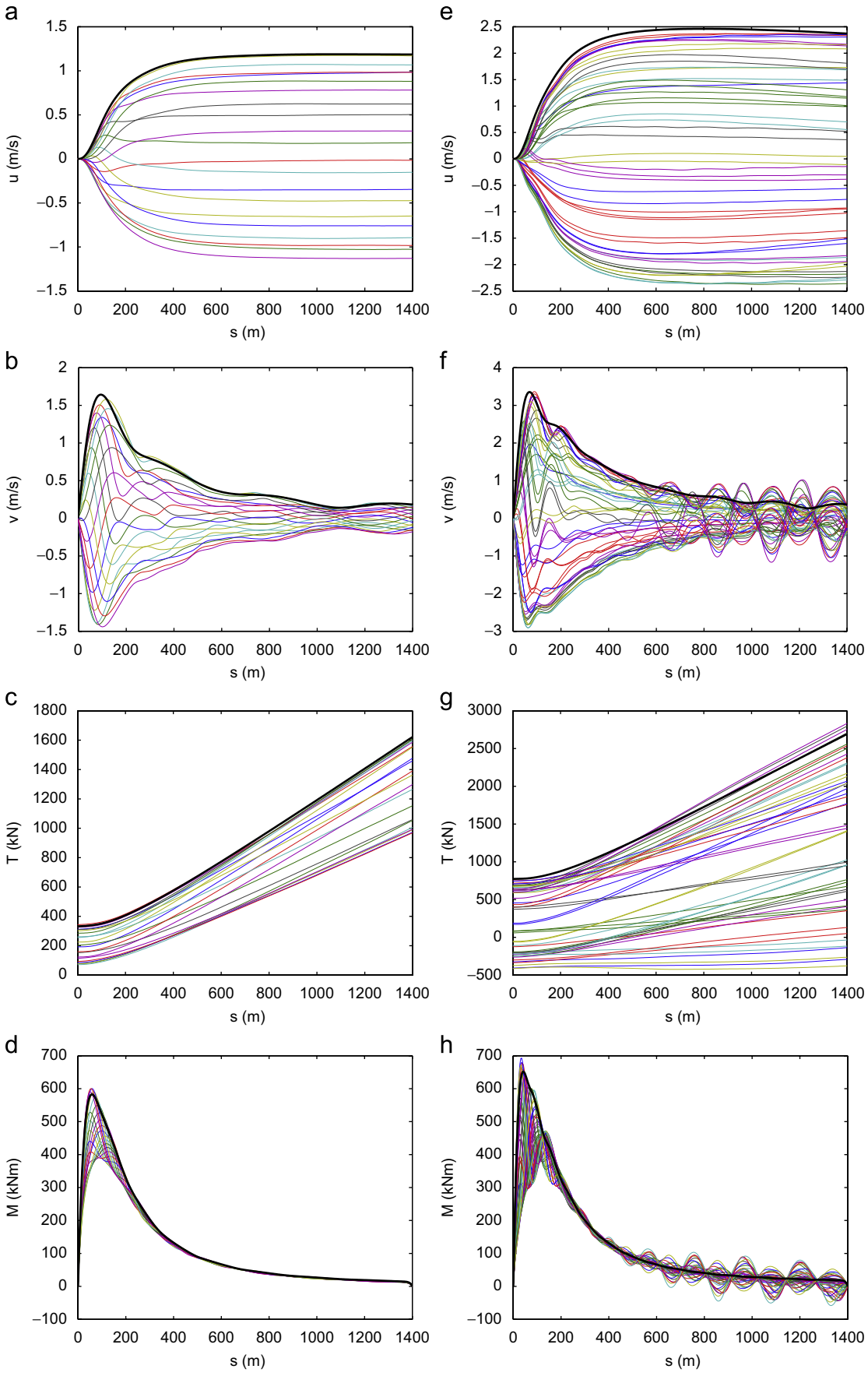

Fig. 22. Comparative results for the riser's dynamic behaviour under *heave* excitation with $z_a = 2$ m amplitude. Snapshots where obtained using the nonlinear solution model and envelope curves through the linearized formulation. Left column corresponds to circular frequency $\omega = 0.6$ rad/s and right column to $\omega = 1.2$ rad/s. Subplots show from top to bottom: axial velocity u, transversal velocity v, total tension T and total bending moment $EI\Omega$.

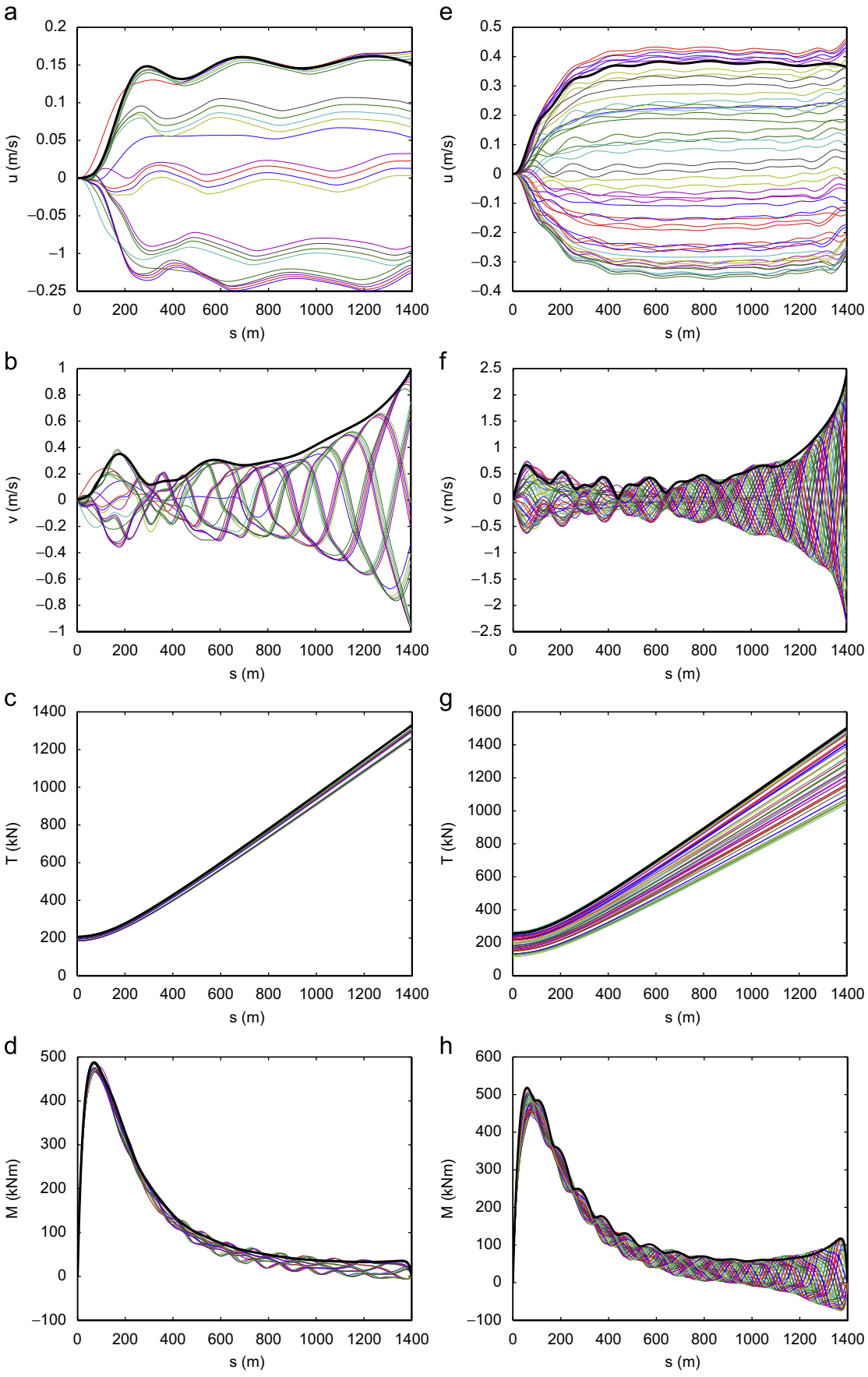

Fig. 23. Comparative results for the riser's dynamic behaviour under *surge* excitation with amplitude $x_a = 2\,\text{m}$. Snapshots where obtained using the nonlinear solution model and envelope curves through the linearized formulation. Left column corresponds to circular frequency $\omega = 0.5\,\text{rad/s}$ and right column to $\omega = 1.2\,\text{rad/s}$. Subplots show from top to bottom: axial velocity u, transversal velocity v, total tension T and total bending moment $EI\Omega$.

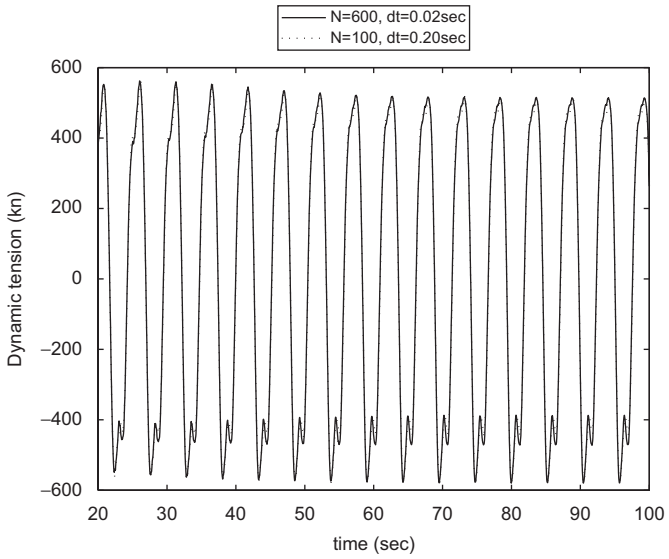

Fig. 24. Convergence of Box method. Comparative calculations for the dynamic tension amplification at the location of the maximum static bending moment. ———— $N = 600$, $\Delta t = 0.020$ s, ----------, $N = 100$, $\Delta t = 0.20$ s. Riser excited by *heave* motions with $z_a = 2$ m and $\omega = 1.2$ rad/s.

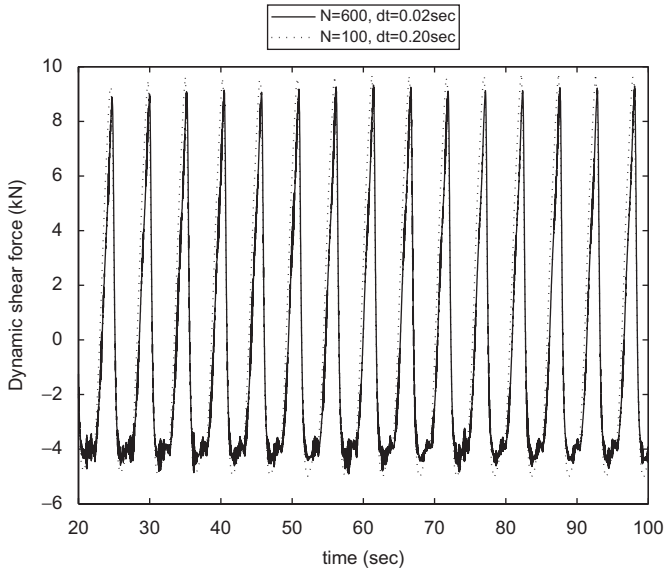

Fig. 25. Convergence of Box method. Comparative calculations for the dynamic shear force amplification at the location of the maximum static bending moment. ———— $N = 600$, $\Delta t = 0.020$ s, ----------, $N = 100$, $\Delta t = 0.20$ s. Riser excited by *heave* motions with $z_a = 2$ m and $\omega = 1.2$ rad/s.

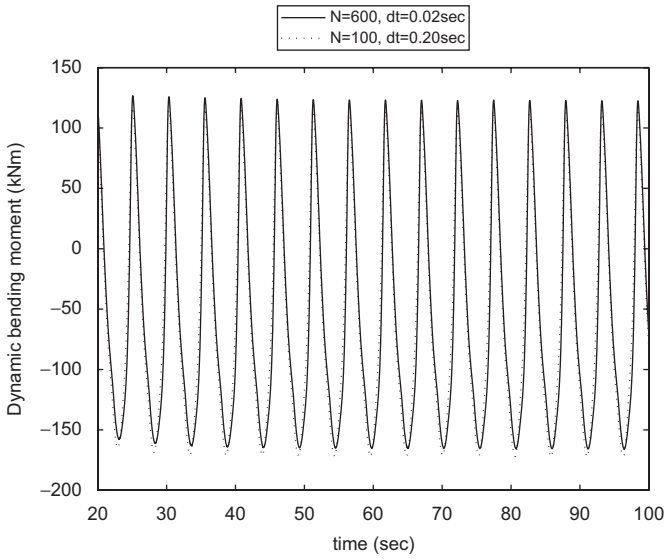

Fig. 26. Convergence of Box method. Comparative calculations for the dynamic bending moment amplification at the location of the maximum static bending moment. ———— $N = 600$, $\Delta t = 0.020$ s, ----------, $N = 100$, $\Delta t = 0.20$ s. Riser excited by *heave* motions with $z_a = 2$ m and $\omega = 1.2$ rad/s.

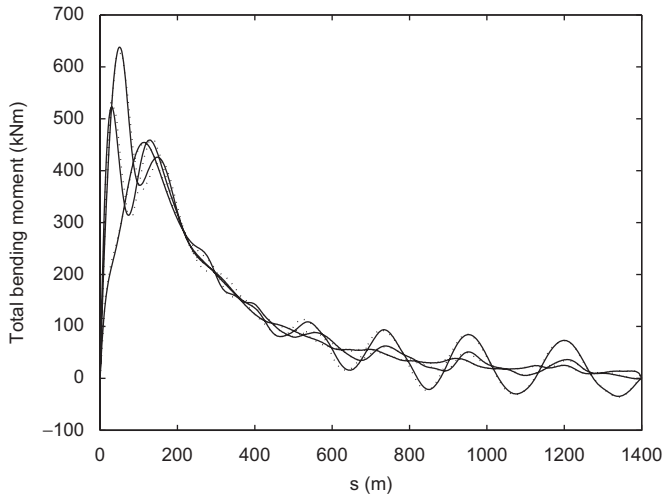

Fig. 27. Convergence of Box method. Comparative calculations for the total bending moment along the structure for three time steps at $t = 30$, 60 and 90 s. ———— $N = 600$, $\Delta t = 0.020$ s, ----------, $N = 100$, $\Delta t = 0.20$ s. Riser excited by *heave* motions with $z_a = 2$ m and $\omega = 1.2$ rad/s.

static configuration of the structure, it is reasonable to consider that the extreme increase in bending moment is the outcome of actions that resemble buckling.

Nevertheless, although the excitation in surge direction is not important with respect to magnitude, the associated dynamic behaviour of the riser, as demonstrated in Figs. 16–21, exhibits very interesting characteristics. In particular, all dynamic terms demonstrate strong variations that cover the complete range of frequencies for both excitation amplitudes. The characteristic wavy trend is less observable in the transfer function of tension and disappears at the end of the range. Furthermore, the agreement between the linear and the nonlinear results is favourable, which in turn implies that the contribution of the geometric nonlinearities to the global behaviour of the structure is relatively insignificant. Small, but noteworthy differences are observed in an unexpected area of excitation frequencies on either side of 0.5 rad/s. The latter finding, however, does not concern all dynamic components examined in the present. Significant discrepancies are detected on the shear force (Fig. 17) and on the angle

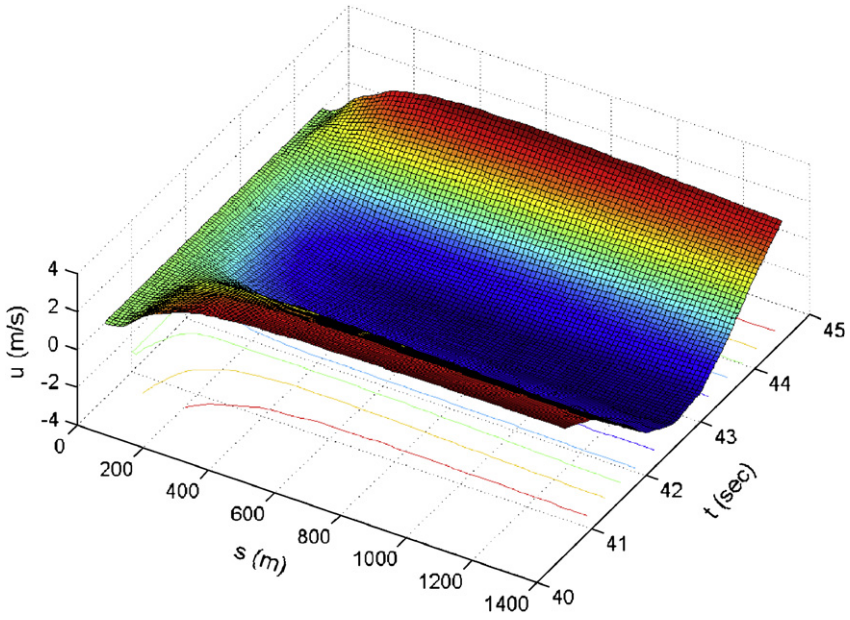

Fig. 28. Axial velocity u along the structure during one simulation period after a steady-state response has been established. Excitation properties: *heave* excitation at the top with amplitude $z_a = 2$ m and circular frequency $\omega = 1.4$ rad/s.

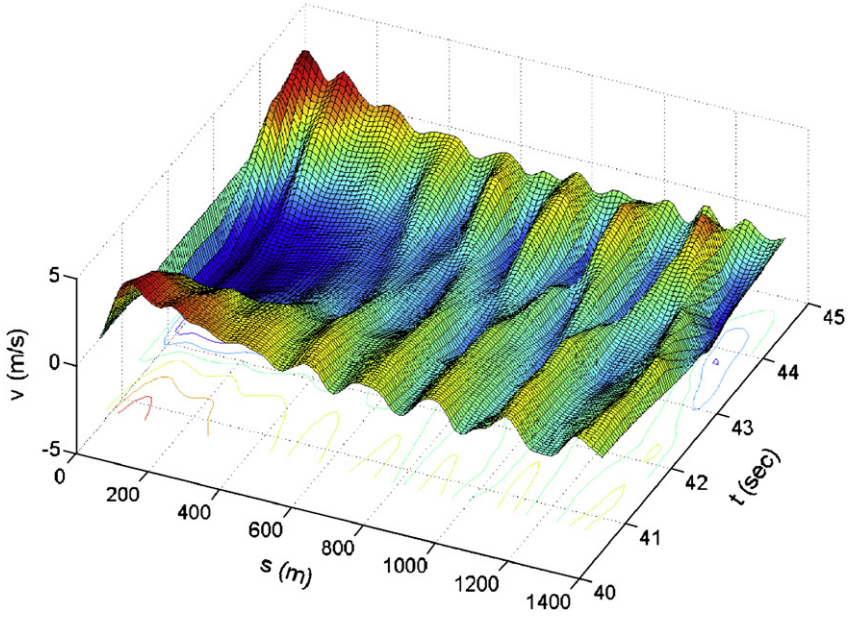

Fig. 29. Transversal velocity v along the structure during one simulation period after a steady-state response has been established. Excitation properties: *heave* excitation at the top with amplitude $z_a = 2$ m and circular frequency $\omega = 1.4$ rad/s.

(Fig. 21), which are not reflected, however, on the transfer functions for the most important variable that influences the safe operation of the riser, i.e. the bending moment (Fig. 20). The pattern for the variation of the dynamic bending moment is provided by the transfer function of the transversal motion (Fig. 19). It is interesting to highlight that contrary to the heave excitation, the maximum bending moment does not follow a steadily increasing path for higher excitation frequencies as the maximum calculated value is in the middle of the range (around 0.8 rad/s).

5.3. Effect of geometric nonlinearities

In general, the contribution of the nonlinear terms becomes substantial for fast motions and large amplitudes. Figs. 22 and 23 correspond to vertical and horizontal excitation, respectively, and show comparative calculations for various dynamic components. These are, the axial velocity $u(s,t)$, the transversal velocity $v(s,t)$, the tension $T(s,t)$ and the bending moment $EI\Omega(s,t)$. The loading components depict total quantities, namely, the summation of the static and the dynamic terms. Two frequencies were

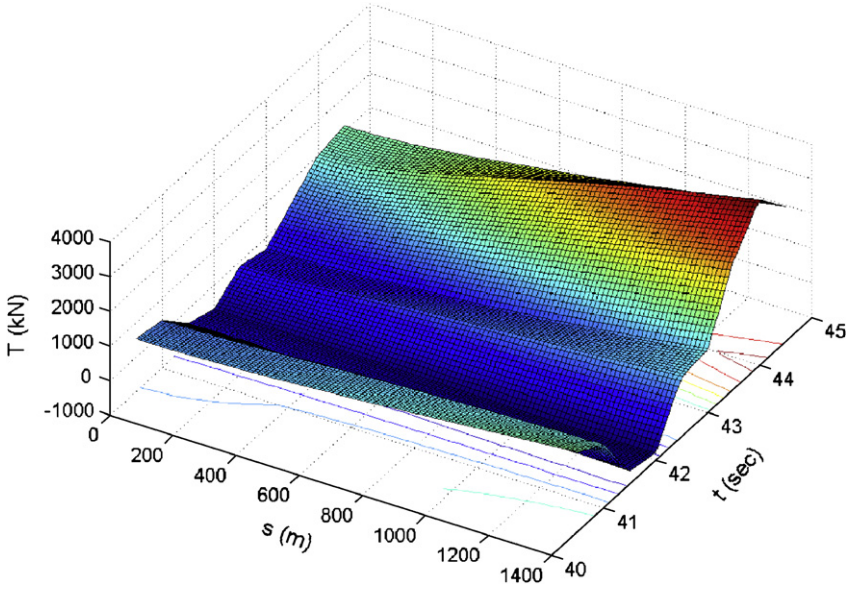

Fig. 30. Total tension T along the structure during one simulation period after a steady-state response has been established. Excitation properties: *heave* excitation at the top with amplitude $z_a = 2\,\text{m}$ and circular frequency $\omega = 1.4\,\text{rad/s}$.

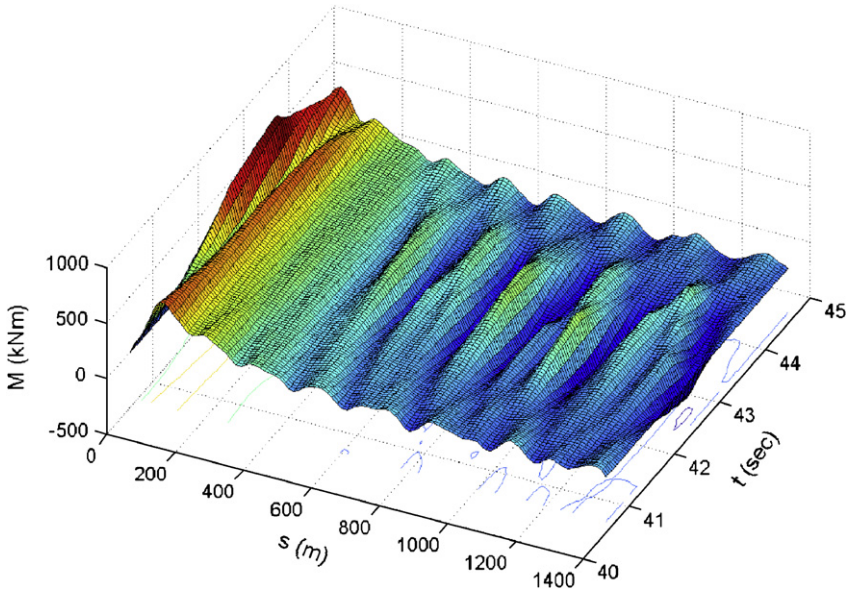

Fig. 31. Total bending moment $EI\Omega$ along the structure during one simulation period after a steady-state response has been established. Excitation properties: *heave* excitation at the top with amplitude $z_a = 2\,\text{m}$ and circular frequency $\omega = 1.4\,\text{rad/s}$.

considered for each orientation; one in the middle and the other at the end of the investigated range, while the amplitude was kept constant and equal to 2 m in both directions. Figs. 22 and 23 have been plotted using the results from both solution models proposed in the present. The snapshots were obtained through nonlinear time domain simulations and show the variation of u, v, T and $EI\Omega$ along the unstretched length of the structure, for one period of the output signals after a steady-state response has been established. The envelope curves demonstrate the amplitude of the response at each point s along the structure. The graphical representation of any envelope curve demonstrates the upper boundary line, which according to the linear approach should not be exceeded by any dynamic component.

According to the data depicted in Figs. 22 and 23 that correspond to slow motions (left columns) the agreement between the linear and the nonlinear calculations is favourable. The envelope curves capture with excellent accuracy the upper variation boundary of the investigated quantities. In addition, the velocity curves in both directions exhibit a symmetric variation with respect to zero (Figs. 22a,b and 23a,b). The latter remarks attest the small to marginal contribution of the nonlinear terms for slow imposed motions. With regard to the severity of loading, it is immediately apparent that the motions in

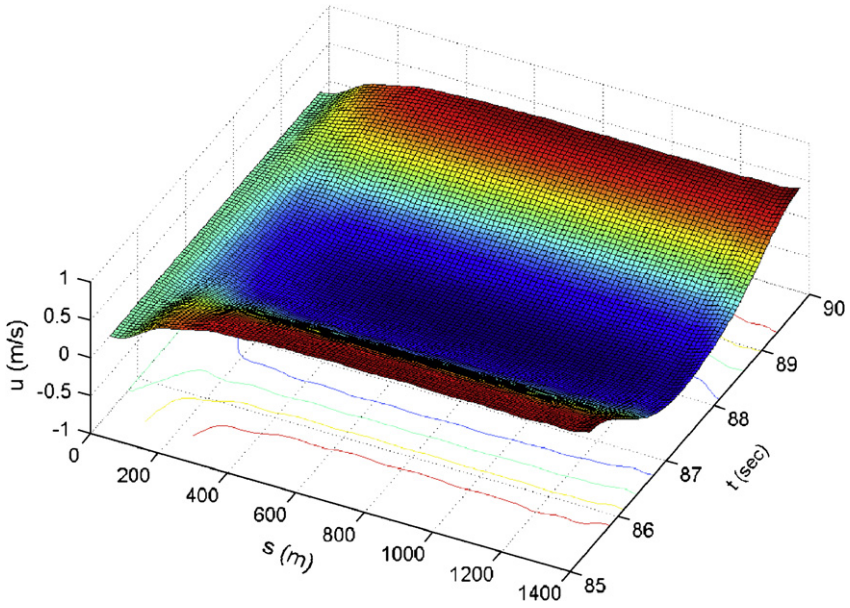

Fig. 32. Axial velocity u along the structure during one simulation period after a steady-state response has been established. Excitation properties: *surge* excitation at the top with amplitude $x_a = 2\,\text{m}$ and circular frequency $\omega = 1.4\,\text{rad/s}$.

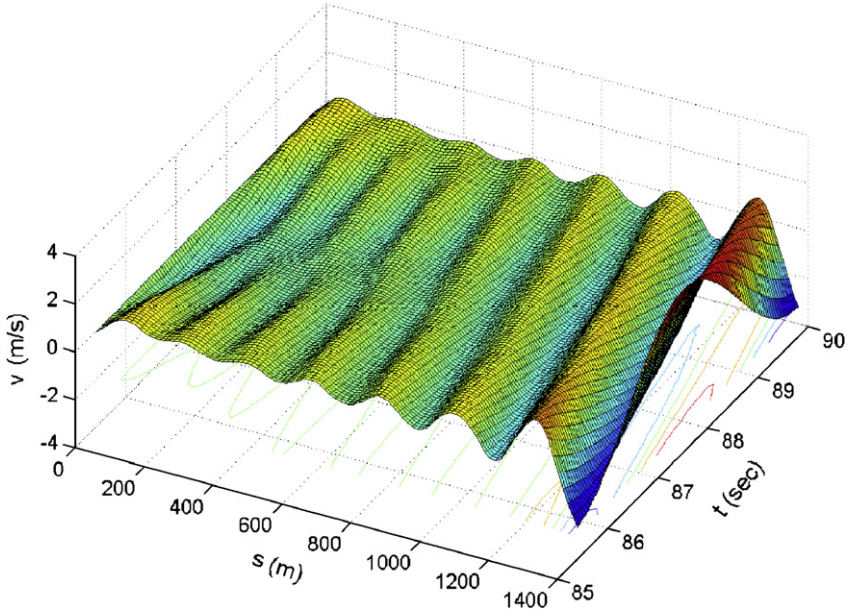

Fig. 33. Transversal velocity v along the structure during one simulation period after a steady-state response has been established. Excitation properties: *surge* excitation at the top with amplitude $x_a = 2\,\text{m}$ and circular frequency $\omega = 1.4\,\text{rad/s}$.

heave direction require particular attention as they result in larger tensions and moments while at the same time the areas which are covered by the snapshots become wider (Figs. 22c,d and 23c,d). For slow horizontal excitations, the effect of any dynamic contribution, both linear and nonlinear, is practically zero as the associated variation curves can be approximated with sufficient accuracy by the static values (see Fig. 2).

The situation deteriorates when faster motions are considered (right columns in Figs. 22 and 23). Nevertheless, differences between the linear and the nonlinear calculations are observed only for the vertical excitation case (Fig. 22). In addition to the increased values of the loading variables, which originate from the fast vertical excitation, there are also several interesting issues which are detected by inspecting Figs. 22f–22h and they deserve further discussion. These are: (a) the strong variation of the transversal velocity (Fig. 22f) at the upper portion of the catenary, which in turn is reflected on the snapshots of the bending moment (Fig. 22h); (b) the snapshots for the tension values go beyond the envelope curve which approximates the linear boundary of the solution; (c) the

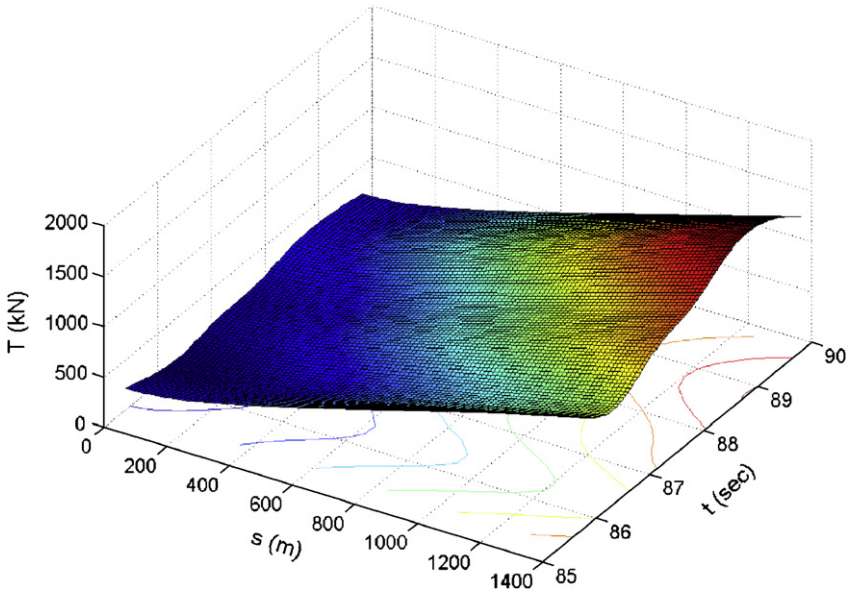

Fig. 34. Total tension T along the structure during one simulation period after a steady-state response has been established. Excitation properties: *surge* excitation at the top with amplitude $x_a = 2\,\mathrm{m}$ and circular frequency $\omega = 1.4\,\mathrm{rad/s}$.

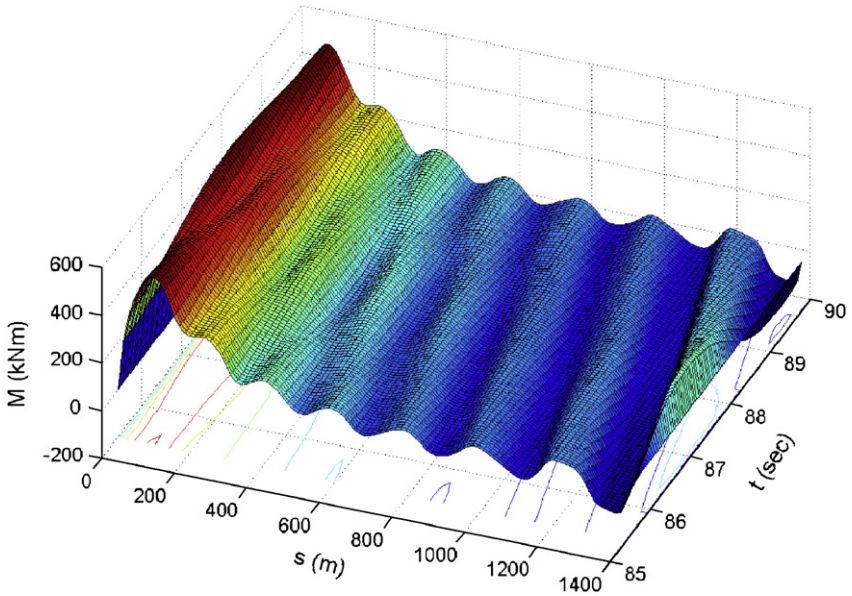

Fig. 35. Total bending moment $EI\Omega$ along the structure during one simulation period after a steady-state response has been established. Excitation properties: *surge* excitation at the top with amplitude $x_a = 2\,\mathrm{m}$ and circular frequency $\omega = 1.4\,\mathrm{rad/s}$.

tension along the structure (Fig. 22g) varies excessively during one period of the steady-state response and there are instances where the tension becomes negative and (d) the previous remark is valid also with respect to the variation of the bending moment; nevertheless, the phenomenon is less important and it is confined to the upper segment of the structure.

The cause of the above is the extreme values of tension which are developed due to the orientation of the excitation. The mechanism that enables these impacts is the coupling between the transversal and the axial motions of the structure. From the mathematical point of view, the nonlinear term, which is primarily responsible for relevant effects, is the tension–curvature geometric nonlinearity $T\Omega$ (see Eq. (2)).

The horizontal excitation case appears to be less effective in terms of the dynamic loading. It should be noted, however, that the specific orientation of the excitation causes a slight wavy variation of the bending moment along the lower-half of the catenary (Fig. 23h) and in addition, the maximum dynamic bending moment occurs just before the top end of the structure and not in the

vicinity of the maximum static bending moment close to the touch-down point.

The conditions, which cause extreme responses where the nonlinear terms play a predominant role, are the most demonstrative for verifying the efficiency of the present solution method. To this end, the stability and the convergence characteristics of the Box approximation are shown through comparative calculations that refer to a relatively heavy loading ($z_a = 2$ m and $\omega = 1.2$ rad/s). The associated numerical results that correspond to two different pairs of spatial and time discretization, i.e. $\Delta s = 2.337$ m, $\Delta t = 0.02$ s and $\Delta s = 14.141$ m, $\Delta t = 0.2$ s are shown in Figs. 24–27. Figs. 24–26 depict the output signals of the dynamic tension, the dynamic shear force and the dynamic bending moment, respectively, at the location of the maximum static bending moment. Fig. 27 shows the variation of the total bending moment along the structure at three indicative time steps. As can be seen the coincidence of the results is excellent which in turn demonstrates the reliability of the solution method even with relatively few discretization elements and relatively large values of Δt. It should be noted, however, that the use of large time steps effectively filters out the higher frequency responses which could lead to loss of important information with regard to the contribution of the geometric nonlinearities. The later remark is immediately apparent in the time histories of the shear force (Fig. 25).

The 3D plots in Figs. 28–35 provide a more descriptive depiction for the dynamics of the continuum system examined in the present subjected to heave (Figs. 28–31) and surge (Figs. 32–35) motions. The variables, which are used for showing the particulars of the dynamic behaviour, are again, the velocities u and v, the tension T and the bending moment $EI\Omega$. These are depicted as functions of independent variables s and t, at all 400 discretization points along the structure and for one period of the steady-state response. The relevant calculations were performed using a sufficiently high frequency (1.4 rad/s) in order to enable stimulation of nonlinear impacts.

According to Figs. 28 and 32 the variation of the axial velocity exhibits the same fashion for both directions of the excitation. The large axial motions, which are encountered in the vertical excitation case, are directly reflected in the function of tension (Fig. 30), which varies between positive and negative value ranges. On the contrary, when the motions are imposed horizontally, the variation of tension is practically insignificant as demonstrated by the level inclined surface that represents $T(s,t)$ (Fig. 34). In the vertical excitation case the geometric nonlinearities become substantial and consequently the coupling between the axial and the transversal oscillations, forces the latter to exhibit the strong fluctuations depicted in Fig. 29. Apparently, the pattern for the bending moment is provided by the transversal motion as can be easily seen by inspecting Figs. 29 and 31 and Figs. 33 and 35. Here, the stronger variation of the bending moment is due to the higher excitation frequency that was used for the calculations. For the vertical excitation case (Fig. 31) the output signal for the bending moment is governed by a sort of abnormal waveforms at the upper part of the structure, while the corresponding response due to motions imposed horizontally is characterized by the almost harmonic configuration as manifested in Fig. 35.

5.4. Nonlinear contributions for small depths

The effect of nonlinearities is known to reduce with increasing water depth. In order to examine the validity of the later remark, additional numerical tests were performed for 100 m water depth. The installation characteristics that determine the static configuration of the shallow water catenary, namely, the pretension, the suspended length and the angle at the top are given in the last column of Table 1 (Model No 3). Fig. 36 shows indicative numerical results that highlight the effect of the nonlinear terms for the reduced water depth of 100 m. The depicted results show the impact of both surge and heave excitation, with a harsh loading according to the imposed amplitude and the frequency of the excitation (x_a, $z_a = 2$ m and $\omega = 1.2$ m/s). Figs. 36a and d do not indicate any profound impact of the nonlinear terms on the transversal motions as the linearized formulation approximates with satisfactory accuracy the actual nonlinear behaviour of the structure. Nevertheless, the tension and the bending moment along the structure appear to be very affected by the nonlinear components of the dynamic equilibrium system. The later remark is more easily seen in Figs. 36b, c, e and f, which show the variation of the tension and the bending moment. The subplots exhibit large differences between the linearized and the actual nonlinear behaviour of the structure. In addition, one can easily observe the long interval where compression loading occurs (Figs. 36b and e), which is responsible for the strong amplification of the bending moment (Figs. 36c and f). It should be mentioned that the differences in the calculated results for the same excitation properties between the linear and the nonlinear model for the long (1400 m length in 1200 m water depth) catenary riser investigated in Section 5.3 were definitely smaller (see Figs. 22 and 23). In addition, for the smaller water depth case examined herein, the absolute maximum of the total bending moment rises up to 1400 kN m for the surge excitation and just before the upper end, and up to 600 kN m for the heave excitation very close to the lower end. These extreme phenomena originate explicitly from the contribution of the geometric nonlinearities the effect of which is distinctly stronger for smaller water depths. Here the surge motion is more important than the heave motion in terms of the development of max bending moments. This is due to the static configuration of the catenary, which for the surge excitation case leads to larger axial components compared to the heave excitation.

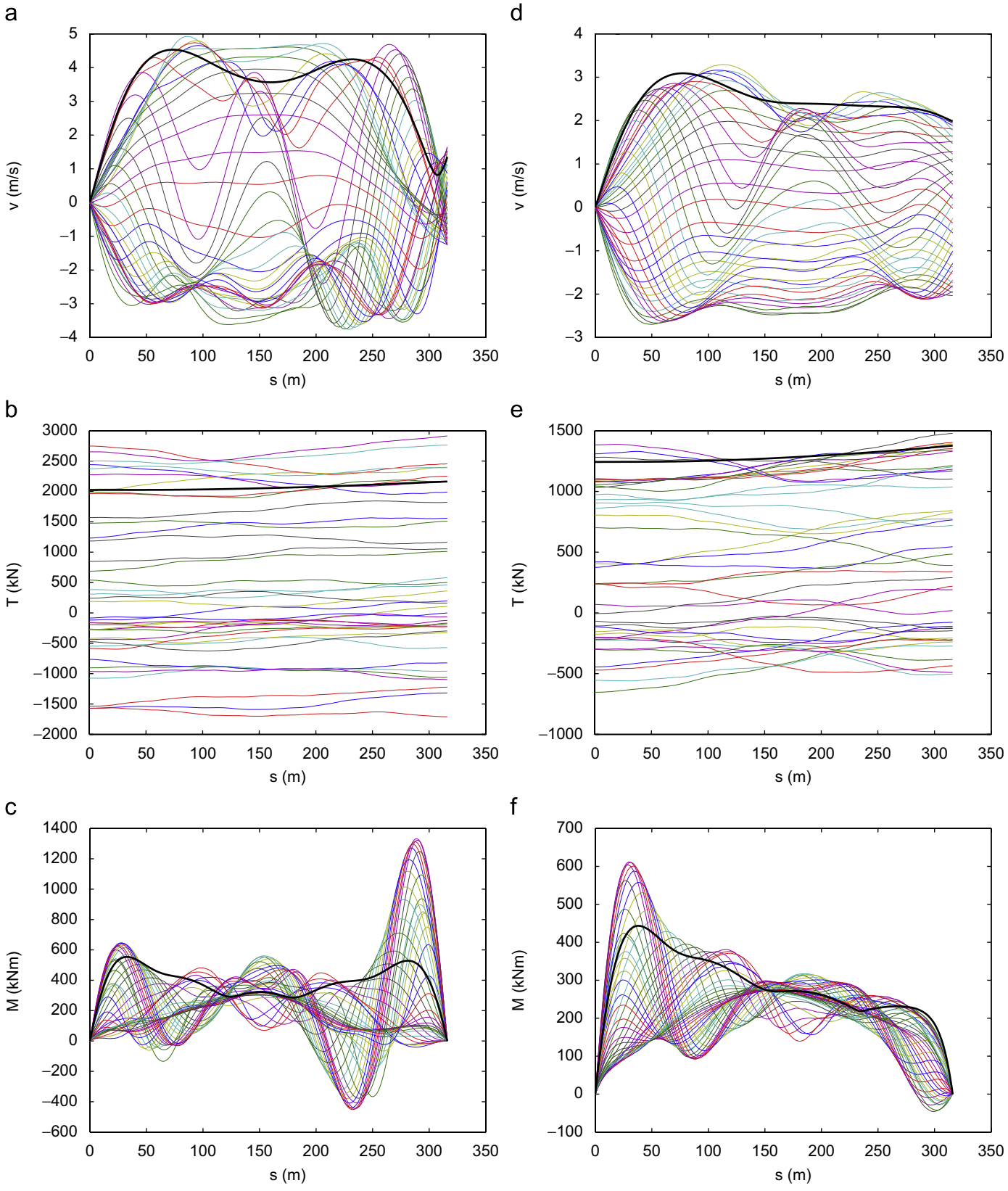

Fig. 36. Comparative results for the riser's dynamic behaviour under *surge* and *heave* excitation in 100 m water depth. Pretension 500 kN, suspended length 316 m, angle at the top 55.7°. Excitation amplitude 2 m and excitation frequency 1.2 rad/s. Snapshots where obtained using the nonlinear solution model and envelope curves through the linearized formulation. Line discretization $N = 400$. Time domain solution achieved using time step $\Delta t = 0.05$ s. Left column corresponds to surge excitation and right column to heave excitation. Subplots depict from top to bottom: transversal velocity v, total tension T and total bending moment $EI\Omega$.

6. Conclusions

This paper dealt with the dynamic equilibrium problem of 2D catenary risers. The method that was proposed for the solution of the associated mathematical formulation was based on a FD scheme that was applied to both the nonlinear and the simplified linear model. The FD method employed for the purposes of the present contribution is unconditionally stable and provides very fast convergence. This was demonstrated through comparative calculations using different physical grid spacing. In addition the proposed solution method does not require the application of a special numerical integration method in the time domain as the equivalent algebraic system is solved simultaneously in terms of the two independent variables of the partial differential equations.

A great part of the numerical predictions concerned the location of the maximum static bending moment. It was found that the heave excitations lead to an incremental amplification of the loading components for increased excitation frequencies while the motions in surge direction cause the strong variation of the same components along the whole frequency range. The contribution of the nonlinear terms appears to be very important for fast displacements in heave direction. Under these conditions the structure is subjected to compression loading due to the fact that the dynamic part of the tension exceeds the static counterpart and there are instances where the total tension becomes negative. This action is subsequently reflected on the total bending moment, which exhibits a strong variation along the upper half of the structure and an excessive increase at the location of the maximum static bending moment in the vicinity of the touch-down point.

Acknowledgements

The author wishes to thank Professor C.M. Larsen and Dr. E. Passano for their support and valuable guidance during author's stay at the Centre of Ships and Offshore Structures at Trondheim, Norway.

Appendix A. Algebraic expansion for the original nonlinear system of dynamic equilibrium

$$\begin{aligned}E_1 = & -\frac{m}{2\Delta t}(u_k^{j+1}+u_{k-1}^{j+1}-u_k^j-u_{k-1}^j)\\ & +\frac{m}{8\Delta t}(v_k^{j+1}+v_{k-1}^{j+1}+v_k^j+v_{k-1}^j)\\ & \times(\phi_k^{j+1}+\phi_{k-1}^{j+1}-\phi_k^j-\phi_{k-1}^j)\\ & +\frac{1}{2\Delta s}(T_k^{j+1}+T_k^j-T_{k-1}^{j+1}-T_{k-1}^j)\\ & -\frac{w_0}{4}(\sin\phi_k^{j+1}+\sin\phi_{k-1}^{j+1}+\sin\phi_k^j+\sin\phi_{k-1}^j)\\ & -\tfrac{1}{4}(\Omega_k^{j+1}Q_k^{j+1}+\Omega_k^jQ_k^j+\Omega_{k-1}^{j+1}Q_{k-1}^{j+1}+\Omega_{k-1}^jQ_{k-1}^j)\\ & -\tfrac{1}{2}\rho\pi C_{\mathrm{dt}}\frac{d}{4}(|u_k^{j+1}|u_k^{j+1}+|u_{k-1}^{j+1}|u_{k-1}^{j+1}\\ & +|u_k^j|u_k^j+|u_{k-1}^j|u_{k-1}^j)=0, \end{aligned}\tag{A.1}$$

$$\begin{aligned}E_2 = & -\frac{(m+m_a)}{2\Delta t}(v_k^{j+1}+v_{k-1}^{j+1}-v_k^j-v_{k-1}^j)\\ & -\frac{m}{8\Delta t}(u_k^{j+1}+u_{k-1}^{j+1}+u_k^j+u_{k-1}^j)\\ & \times(\phi_k^{j+1}+\phi_{k-1}^{j+1}-\phi_k^j-\phi_{k-1}^j)\\ & +\frac{1}{2\Delta s}(Q_k^{j+1}+Q_k^j-Q_{k-1}^{j+1}-Q_{k-1}^j)\\ & -\frac{w_0}{4}(\cos\phi_k^{j+1}+\cos\phi_{k-1}^{j+1}+\cos\phi_k^j+\cos\phi_{k-1}^j)\\ & +\frac{1}{4}(\Omega_k^{j+1}T_k^{j+1}+\Omega_k^jT_k^j+\Omega_{k-1}^{j+1}T_{k-1}^{j+1}+\Omega_{k-1}^jT_{k-1}^j)\\ & -\frac{1}{2}\rho C_{\mathrm{dn}}\frac{d}{4}(|v_k^{j+1}|v_k^{j+1}+|v_{k-1}^{j+1}|v_{k-1}^{j+1}\\ & +|v_k^j|v_k^j+|v_{k-1}^j|v_{k-1}^j)=0, \end{aligned}\tag{A.2}$$

$$\begin{aligned}E_3 = & -\frac{1}{2\Delta t}(T_k^{j+1}+T_{k-1}^{j+1}-T_k^j-T_{k-1}^j)\\ & +\frac{EA}{2\Delta s}(u_k^{j+1}+u_k^j-u_{k-1}^{j+1}-u_{k-1}^j)\\ & -\frac{EA}{4}(\Omega_k^{j+1}v_k^{j+1}+\Omega_k^jv_k^j\\ & +\Omega_{k-1}^{j+1}v_{k-1}^{j+1}+\Omega_{k-1}^jv_{k-1}^j)=0, \end{aligned}\tag{A.3}$$

$$\begin{aligned}E_4 = & -\frac{1}{2\Delta t}(\phi_k^{j+1}+\phi_{k-1}^{j+1}-\phi_k^j-\phi_{k-1}^j)\\ & +\frac{1}{2\Delta s}(v_k^{j+1}+v_k^j-v_{k-1}^{j+1}-v_{k-1}^j)\\ & +\frac{1}{4}(\Omega_k^{j+1}u_k^{j+1}+\Omega_k^ju_k^j\\ & +\Omega_{k-1}^{j+1}u_{k-1}^{j+1}+\Omega_{k-1}^ju_{k-1}^j)=0, \end{aligned}\tag{A.4}$$

$$E_5=\frac{EI}{\Delta s}(\Omega_k^{j+1}-\Omega_{k-1}^{j+1})+\frac{1}{2}(Q_k^{j+1}+Q_{k-1}^{j+1})=0,\tag{A.5}$$

$$E_6=\frac{1}{\Delta s}(\phi_k^{j+1}-\phi_{k-1}^{j+1})-\frac{1}{2}(\Omega_k^{j+1}+\Omega_{k-1}^{j+1})=0.\tag{A.6}$$

Appendix B. Algebraic expansion for the equivalent linearized formulation of the dynamic equilibrium problem

$$\begin{aligned}LE_1 = & \frac{2}{\Delta s}(\widetilde{T}_k^{(\mathrm{r})}-\widetilde{T}_{k-1}^{(\mathrm{r})})-w_0(\cos\overline{\phi}_k\widetilde{\phi}_k^{(\mathrm{r})}+\cos\overline{\phi}_{k-1}\widetilde{\phi}_{k-1}^{(\mathrm{r})})\\ & -(\overline{Q}_k\widetilde{\Omega}_k^{(\mathrm{r})}+\overline{Q}_{k-1}\widetilde{\Omega}_{k-1}^{(\mathrm{r})})-(\overline{\Omega}_k\widetilde{Q}_k^{(\mathrm{r})}+\overline{\Omega}_{k-1}\widetilde{Q}_{k-1}^{(\mathrm{r})})\\ & +\omega^2m(p_k^{(\mathrm{r})}+p_{k-1}^{(\mathrm{r})})=0, \end{aligned}\tag{B.1}$$

$$\begin{aligned}LE_2 = & \frac{2}{\Delta s}(\widetilde{T}_k^{(\mathrm{i})}-\widetilde{T}_{k-1}^{(\mathrm{i})})-w_0(\cos\overline{\phi}_k\widetilde{\phi}_k^{(\mathrm{i})}+\cos\overline{\phi}_{k-1}\widetilde{\phi}_{k-1}^{(\mathrm{i})})\\ & -(\overline{Q}_k\widetilde{Q}_k^{(\mathrm{i})}+\overline{Q}_{k-1}\overline{\Omega}_{k-1}^{(\mathrm{i})})-(\overline{\Omega}_k\tilde{Q}_k^{(\mathrm{i})}+\overline{\Omega}_{k-1}\widetilde{Q}_{k-1}^{(\mathrm{i})})\\ & +\omega^2m(p_k^{(\mathrm{i})}+p_{k-1}^{(\mathrm{i})})=0, \end{aligned}\tag{B.2}$$

$$LE_3 = \frac{2}{\Delta s}(\widetilde{Q}_k^{(\mathrm{r})} - \widetilde{Q}_{k-1}^{(\mathrm{r})}) + w_0(\sin\overline{\phi}_k\widetilde{\phi}_k^{(r)} + \sin\overline{\phi}_{k-1}\widetilde{\phi}_{k-1}^{(\mathrm{r})}) + (\overline{T}_k\widetilde{Q}_k^{(\mathrm{r})} + \overline{T}_{k-1}\widetilde{\Omega}_{k-1}^{(\mathrm{r})}) + (\overline{\Omega}_k\widetilde{T}_k^{(\mathrm{r})} + \overline{\Omega}_{k-1}\widetilde{T}_{k-1}^{(\mathrm{r})}) + \omega^2(m+m_a)(q_k^{(\mathrm{r})} + q_{k-1}^{(\mathrm{r})}) + b_0\omega^2(|q_k|q_k^{(\mathrm{i})} + |q_{k-1}|q_{k-1}^{(\mathrm{i})}) = 0, \quad (B.3)$$

$$LE_4 = \frac{2}{\Delta s}(\widetilde{Q}_k^{(\mathrm{i})} - \widetilde{Q}_{k-1}^{(\mathrm{i})}) + w_0(\sin\overline{\phi}_k\widetilde{\phi}_k^{(\mathrm{i})} + \sin\overline{\phi}_{k-1}\widetilde{\phi}_{k-1}^{(\mathrm{i})}) + (\overline{T}_k\widetilde{\Omega}_k^{(\mathrm{i})} + \overline{T}_{k-1}\widetilde{\Omega}_{k-1}^{(\mathrm{i})}) + (\overline{\Omega}_k\tilde{T}_k^{(\mathrm{i})} + \overline{\Omega}_{k-1}\tilde{T}_{k-1}^{(\mathrm{i})}) + \omega^2(m+m_a)(q_k^{(\mathrm{i})} + q_{k-1}^{(\mathrm{i})}) - b_0\omega^2(|q_k|q_k^{(\mathrm{r})} + |q_{k-1}|q_{k-1}^{(\mathrm{r})}) = 0, \quad (B.4)$$

$$LE_5 = 2\frac{EA}{\Delta s}(p_k^{(\mathrm{r})} - p_{k-1}^{(\mathrm{r})}) - EA(\overline{\Omega}_k q_k^{(\mathrm{r})} + \overline{\Omega}_{k-1}q_{k-1}^{(\mathrm{r})}) - (\widetilde{T}_k^{(\mathrm{r})} + \widetilde{T}_{k-1}^{(\mathrm{r})}) = 0, \quad (B.5)$$

$$LE_6 = 2\frac{EA}{\Delta s}(p_k^{(\mathrm{i})} - p_{k-1}^{(\mathrm{i})}) - EA(\overline{\Omega}_k q_k^{(\mathrm{i})} + \overline{\Omega}_{k-1}q_{k-1}^{(\mathrm{i})}) - (\widetilde{T}_k^{(\mathrm{i})} + \widetilde{T}_{k-1}^{(\mathrm{i})}) = 0, \quad (B.6)$$

$$LE_7 = \frac{2}{\Delta s}(q_k^{(\mathrm{r})} - q_{k-1}^{(\mathrm{r})}) + (\overline{\Omega}_k p_k^{(\mathrm{r})} + \overline{\Omega}_{k-1}p_{k-1}^{(\mathrm{r})}) - (\widetilde{\phi}_k^{(\mathrm{r})} + \widetilde{\phi}_{k-1}^{(\mathrm{r})}) = 0, \quad (B.7)$$

$$LE_8 = \frac{2}{\Delta s}(q_k^{(\mathrm{i})} - q_{k-1}^{(\mathrm{i})}) + (\overline{\Omega}_k p_k^{(\mathrm{i})} + \overline{\Omega}_{k-1}p_{k-1}^{(\mathrm{i})}) - (\widetilde{\phi}_k^{(\mathrm{i})} + \widetilde{\phi}_{k-1}^{(\mathrm{i})}) = 0, \quad (B.8)$$

$$LE_9 = \frac{2}{\Delta s}(\widetilde{\Omega}_k^{(\mathrm{r})} - \widetilde{\Omega}_{k-1}^{(\mathrm{r})}) + \frac{1}{EI}(\widetilde{Q}_k^{(\mathrm{r})} + \widetilde{Q}_{k-1}^{(\mathrm{r})}) = 0, \quad (B.9)$$

$$LE_{10} = \frac{2}{\Delta s}(\widetilde{\Omega}_k^{(\mathrm{i})} - \widetilde{\Omega}_{k-1}^{(\mathrm{i})}) + \frac{1}{EI}(\widetilde{Q}_k^{(\mathrm{i})} + \widetilde{Q}_{k-1}^{(\mathrm{i})}) = 0, \quad (B.10)$$

$$LE_{11} = \frac{2}{\Delta s}(\widetilde{\phi}_k^{(\mathrm{r})} - \widetilde{\phi}_{k-1}^{(\mathrm{r})}) - (\widetilde{\Omega}_k^{(\mathrm{r})} + \widetilde{\Omega}_{k-1}^{(\mathrm{r})}) = 0, \quad (B.11)$$

$$LE_{12} = \frac{2}{\Delta s}(\widetilde{\phi}_k^{(\mathrm{i})} - \widetilde{\phi}_{k-1}^{(\mathrm{i})}) - (\widetilde{\Omega}_k^{(\mathrm{i})} + \widetilde{\Omega}_{k-1}^{(\mathrm{i})}) = 0. \quad (B.12)$$

References

Ablow, C.M., Schechter, S., 1983. Numerical simulation of undersea cable dynamics. Ocean Engineering 10 (6), 443–457.

Burgess, J.J., 1993. Bending stiffness in a simulation of undersea cable deployment. International Journal of Offshore and Polar Engineering 3 (3), 197–204.

Chai, Y.T., Varyani, K.S., 2006. An absolute coordinate formulation for three-dimensional flexible pipe analysis. Ocean Engineering 33, 23–58.

Chatjigeorgiou, I.K., 2004. On the parametric excitation of vertical elastic slender structures and the effect of damping in marine applications. Applied Ocean Research 26, 23–33.

Chatjigeorgiou, I.K., Passano, E., Larsen, C.M., 2007. Extreme bending moments on long catenary risers due to heave excitation. In: Proceedings of the 26th International Conference on Offshore Mechanics and Arctic Engineering (OMAE 2007), San Diego, California, USA. Paper No 29384.

Dareing, D.W., Neathering, R.F., 1970. Finite differences technique for pipeline analysis. Journal of Engineering for Industry, Transactions of the ASME 827–836.

Fylling, I., Larsen, C.M., Sødahl, N., Passano, E., Bech, A., Engseth, A.G., Lie, E., Ormberg, H., 1998. Riflex user's manual. Marintek Report, Trondheim, Norway.

Hoffman, J.D., 1993. Numerical Methods for Engineers and Scientists. McGraw-Hill, New York.

Howell, C.T., 1991. Numerical analysis of 2-D nonlinear cable equations with applications to low tension problems. In: Proceedings of the 1st International Offshore and Polar Engineering Conference (ISOPE 1991), vol. II, Edinburgh, United Kingdom, pp. 203–209.

Jain, A.K., 1994. Review of flexible risers and articulated storage systems. Ocean Engineering 21, 733–750.

McNamara, J.F., O' Brien, P.J., Gilroy, S.G., 1988. Non-linear analysis of flexible risers using hybrid finite elements. Journal of Offshore Mechanics and Arctic Engineering 110 (3), 197–204.

Milinazzo, F., Wilkie, M., Latchman, S.A., 1987. An efficient algorithm for simulating the dynamics of towed cable systems. Ocean Engineering 14 (6), 513–526.

Passano, E., 2007. Personal communication.

Passano, E., Larsen, C.M., 2006. Efficient analysis of a catenary riser. In: Proceedings of the 25th International Conference on Offshore Mechanics and Arctic Engineering (OMAE 2006), Hamburg, Germany, OMAE2006-92308.

Patel, H.M., Seyed, F.B., 1995. Review of flexible risers modelling and analysis techniques. Engineering Structures 17, 293–304.

Pesce, C.P., Fujarra, A.L.C., Simos, A.N., Tannuri, E.A., 1999. Analytical and closed form solutions for deep water riser-like eigenvalue problem. In: Proceedings of the 9th International Offshore and Polar Engineering Conference (ISOPE 1999), vol. II, Brest, France, pp. 255–263.

Pesce, C.P., Martins, C.A., Silveira, L.K.Y., 2006. Riser–soil interaction: local dynamics at TDP and a discussion on the eigenvalue and the VIV problems. Journal of Offshore Mechanics and Arctic Engineering 128, 39–55.

Press, W.H., Flannery, B.P., Teukolsky, S.A., Vetterling, W.T., 1986. Numerical Recipes. Cambridge University Press, Cambridge.

Tjavaras, A.A., Zhu, Q., Liu, Y., Triantafyllou, M.S., Yue, D.K.P., 1998. The mechanics of highly extensible cables. Journal of Sound and Vibration 213 (4), 709–737.

Trianrafyllou, M.S., 1994. Cable mechanics for moored floating structures. In: Proceedings of the 7th International Conference on the Behaviour of Offshore Structures (BOSS 1994), vol. 2, Boston, Massachusetts, pp. 57–77.

Zare, K., Datta, T.K., 1988. Vibration of Lazy-"S" risers due to vortex shedding under lock-in. In: Proceedings of the 20th Offshore Technology Conference, OTC 5795, pp. 451–458.